H3K4me2 distinguishes a distinct class of enhancers during the maternal-to-zygotic transition

Matthew D. Hurton[1], Jennifer M. Miller[1], Miler T. Lee[1,†]

[1]Department of Biological Sciences, University of Pittsburgh, Pittsburgh PA 15213 U.S.A.

[†]To whom correspondence should be addressed: miler@pitt.edu

Abstract

After egg fertilization, an initially silent embryonic genome is transcriptionally activated during the maternal-to-zygotic transition. In zebrafish, maternal vertebrate pluripotency factors Nanog, Pou5f3 (OCT4 homolog), and Sox19b (SOX2 homolog) (NPS) play essential roles in orchestrating embryonic genome activation, acting as “pioneers” that open condensed chromatin and mediate acquisition of activating histone modifications. However, some embryonic gene transcription still occurs in the absence of these factors, suggesting the existence of other mechanisms regulating genome activation. To identify chromatin signatures of these unknown pathways, we profiled the histone modification landscape of zebrafish embryos using CUT&RUN. Our regulatory map revealed two subclasses of enhancers distinguished by presence or absence of H3K4me2. Enhancers lacking H3K4me2 tend to require NPS factors for de novo activation, while enhancers bearing H3K4me2 are epigenetically bookmarked by DNA hypomethylation to recapitulate gamete activity in the embryo, independent of NPS pioneering. Thus, parallel enhancer activation pathways combine to induce transcriptional reprogramming to pluripotency in the early embryo.

Introduction

In animals, embryonic development begins with a transcriptionally silent zygotic genome under the control of maternally deposited RNAs and proteins (Lee et al., 2014; Vastenhouw et al., 2019). In fast-dividing embryos of taxa such as Drosophila, Xenopus, and zebrafish, embryonic chromatin transforms over the course of several cleavages during the maternal-to-zygotic transition (MZT), leading to transcriptional competence and zygotic (embryonic) genome activation (ZGA) in the blastula (Blythe and Wieschaus, 2016; Esmaeili et al., 2020; Liu et al., 2018; Phelps et al., 2023). Genome activation is facilitated in part by maternally deposited transcription factors that bind gene-proximal promoters and gene-distal enhancers in the embryonic genome (Colonnetta et al., 2021; Duan et al., 2021; Gaskill et al., 2021; Gentsch et

al., 2019; Liang et al., 2008; Paraiso et al., 2019; Phelps et al., 2023; ten Bosch et al., 2006). In zebrafish, maternal Nanog, Pou5f3, and Sox19b (NPS) – homologs of the mammalian pluripotency factors NANOG, OCT4, and SOX2 – are essential for regulating a large proportion of genome activation (M. T. Lee et al., 2013; Leichsenring et al., 2013; Miao et al., 2022), thus mechanistically linking mammalian pluripotency induction and the zebrafish MZT.

NPS, like their mammalian counterparts, act as pioneer factors capable of binding DNA regulatory sequences in the context of condensed chromatin (Gao et al., 2022; Liu et al., 2018; Miao et al., 2022; Pálfy et al., 2019; Riesle et al., 2023; Veil et al., 2019), which tends to occlude binding of non pioneers (Barral and Zaret, 2024; Soufi et al., 2015). Binding induces increased chromatin accessibility, leading to the acquisition of activating histone post-translational modifications such as acetylation and H3 lysine 4 (H3K4) methylation, which are correlated with the onset of embryonic gene transcription (Chan et al., 2019; Miao et al., 2022). However, a triple maternal-zygotic mutant for *nanog*, *pou5f3* and *sox19b* (MZ*nps*) still activates some genes, implicating other unknown mechanisms that act alongside of NPS to regulate genome activation (Miao et al., 2022).

Chromatin is dynamic in the early zebrafish embryo. During the first two hours post fertilization (h.p.f.), chromatin is tightly condensed and mostly lacks histone modifications (Lindeman et al., 2011; Liu et al., 2018; Pálfy et al., 2019; Vastenhouw et al., 2010; Zhang et al., 2018). Subsequently, a minor wave of genome activation begins, focused on a small number of gene promoters including the tandemly repeated microRNA *mir-430* encoding locus (Hadzhiev et al., 2023; Heyn et al., 2014). Chromatin accessibility and activating histone modifications have started to emerge, increasing by 4 h.p.f. (sphere stage) to tens of thousands of accessible, highly histone-modified promoters and enhancers (Bogdanovic et al., 2012; Lindeman et al., 2011; Liu et al., 2018; Pálfy et al., 2019; Vastenhouw et al., 2010; Zhang et al., 2014; Zhu et al., 2019). By this point, the major wave of genome activation is underway, involving transcription of >7,000 genes, some of which are de novo expressed in the embryo (strictly zygotic), but the majority of which were already represented in the embryonic transcriptome from the maternal contribution (maternal-zygotic) (Harvey et al., 2013; M. T. Lee et al., 2013).

Many of these chromatin changes require NPS pioneering, but several studies also implicate differential DNA methylation as being instructive for genome activation (Hickey et al., 2022; Jiang et al., 2013; Kaaij et al., 2016; Lee et al., 2015; Liu et al., 2018; Murphy et al., 2018; Potok et al., 2013; Wu et al., 2021; Zhang et al., 2018). Both gametes contribute selectively 5-methylcytosine modified DNA, though rather than establishing differential parent-of-origin imprinted patterns like mice, zebrafish embryonic genome methylation is largely reprogrammed

to match the paternal pattern by 3 h.p.f., through enzymatic-mediated methylation at some loci and passive demethylation at others (Jiang et al., 2013; Potok et al., 2013). Promoters that acquire or sustain hypomethylation recruit “placeholder” nucleosomes, characterized by H3K4 monomethylation (H3K4me1) and the histone variant H2A.Z (H2AFV in zebrafish), which help maintain hypomethylation and chromatin accessibility (Murphy et al., 2018). Hypomethylation at distal regulatory regions is also associated with dynamic regulation, though so far such regions have been found to co-occur with repressive histone modifications like H3K27me3 and H2Aub and thus may represent poised enhancers with roles later in development (Hickey et al., 2022; Kaaij et al., 2016).

These observations implicate a combinatorial regulatory code underlying genome activation that may be further elucidated with additional characterization of embryonic chromatin. There are >100 different histone modifications described thus far (Zhao and Garcia, 2015), the vast majority of which are understudied in any context let alone in embryos. Recent work in mouse embryonic stem cells (mESCs) demonstrates that acetylation of the histone H2B N-terminal tail (H2BNTac) is strongly characteristic of enhancers as compared to most promoters (Narita et al., 2023). Additionally, although most of the focus in gene regulation literature has been on modifications of histone tails, acetylation in the core globular domain of histone H3 has recently been associated with enhancers as well. H3K56ac was shown to co-occur with Oct4 binding in mESCs (Tan et al., 2013), while H3K122ac and H3K64ac appear to mark a set of active enhancers lacking H3K27ac enrichment (Pradeepa et al., 2016). To our knowledge, these marks have not previously been evaluated in zebrafish.

Finally, H3K4 methylation has already been extensively profiled, but the logic dictating methylation degree at regulatory elements – i.e., mono-, di-, or tri-methylation – still needs to be more fully elucidated (Wang and Helin, 2024). Classically, H3K4me3 has been associated with active transcription and is found promoter-proximal in gene bodies, while H3K4me1 and to some extent H3K4me2 is more diagnostic of enhancers (Barski et al., 2007; Ernst et al., 2011; Heintzman et al., 2007; Zentner et al., 2011). Some studies have also found H3K4me3 at enhancers in certain contexts (Barski et al., 2007; Hu et al., 2017; Koch and Andrau, 2011; Liu et al., 2024; Pekowska et al., 2011); however, a recent analysis of several widely used H3K4 methylation antibodies has revealed a high prevalence of cross reactivity, calling into question the extent to which specific methylation degrees can be conclusively deduced at different regulatory elements (Shah et al., 2018). Indeed, using new SNAP-ChIP verified antibodies, only H3K4me1 and H3K4me2, but not H3K4me3, are observed at enhancers in K562 cells (Shah et

al., 2018). These results motivate the re-evaluation of H3K4 methylation status in other systems.

Here, we have mapped the genome-wide distribution of 10 different histone modifications in the early zebrafish embryo using Cleavage Under Targets and Release Using Nuclease (CUT&RUN), to capture signatures of differentially-regulated enhancers and promoters during genome activation. We observe that characteristic combinations of these histone modifications broadly separate putative enhancers and promoters, but we also find that H3K4me2 and not H3K4me3 specifically marks a subclass of active enhancers, distinguishing them from other enhancers bearing only H3K4me1. Both H3K4me1 and H3K4me2-marked enhancers can distally regulate gene transcription. However, H3K4me1 enhancers largely rely on NPS pioneering to gain activity, whereas H3K4me2 enhancer activation is correlated with DNA hypomethylation that reflects their prior activity in gametes. Our findings reveal that differential H3K4me2 can distinguish enhancers subtypes, and that parallel pathways for enhancer activation underlie embryonic genome activation, explaining how some genes can still be activated in the absence of NPS pluripotency factors.

Results

CUT&RUN effectively maps histone modifications in zebrafish blastulae

We adapted and optimized CUT&RUN to zebrafish blastulae as a low-input alternative to conventional chromatin immunoprecipitation sequencing (ChIP-seq) (Akdogan-Ozdilek et al., 2022; Hainer et al., 2019; Skene and Henikoff, 2017). We profiled embryos at the onset of dome stage – 4 to 4.3 h.p.f., the tail end of the major wave of genome activation (Fig 1A) – to assay the histone tail acetylation modifications H3K9ac, H3K27ac, H4K16ac, and H2BK16ac (an example of H2BNTac); the non-tail H3K56ac, H3K64ac, and H3K122ac modifications of the H3 histone globular core; and H3K4me1, 2, and 3 using SNAP-ChIP verified antibodies to precisely distinguish between methylation degrees (Fig 1B) (Supp. Table 1). Only 10 embryos per sample (~70,000 cells (Joseph et al., 2017)) were required to generate robust CUT&RUN libraries. We centered our analyses on genomic intervals flanking accessible chromatin as determined by ATAC-seq from two previously published studies (Liu et al., 2018; Pálfy et al., 2019) (N = 48,395 open-chromatin regions), many of which likely represent active gene regulatory elements in the embryo (Fig 1B). To identify correlated histone mark enrichment patterns across the regions, we performed a principal component analysis (PCA) (Fig 1C-E, Supp. Fig 1A-C). The first two principal components captured 49% of the variation and broadly separate promoters – defined as open regions overlapping Ensembl, RefSeq, and UMMS (Lawson et al.,

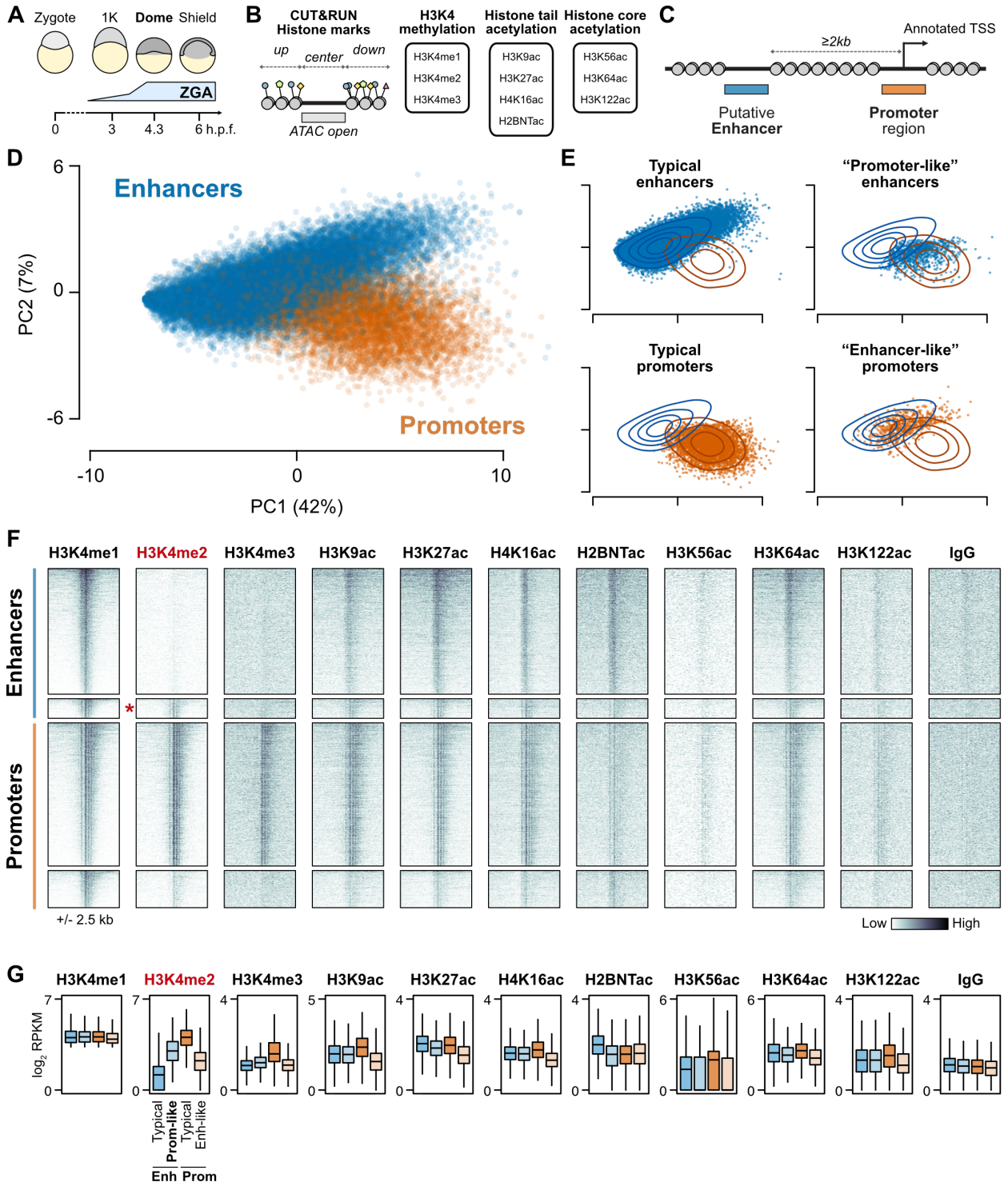

Figure 1. Histone modifications distinguish regulatory elements during the maternal-to-zygotic transition. (A) *Schematic of early zebrafish embryogenesis spanning the 1-cell zygote, 1K-cell, dome, and shield stages, showing the timing of zygotic genome activation (ZGA). h.p.f. = hours post fertilization.* ***(B)*** *CUT&RUN read coverage was measured on open chromatin regions defined by ATAC-seq and adjacent 500-bp upstream and downstream regions for 10 histone modifications.* ***(C)*** *Open chromatin regions were classified as TSS-overlapping promoters or TSS-distal putative enhancers. (cont'd...)*

(...cont'd) ***(D)*** *Biplot of the first two principal components (PCs) of a PCA performed on histone modification coverage on open chromatin regions. Points are labeled blue for enhancers, orange for promoters, as defined in (C). Percent of total variance explained per PC in parentheses.* ***(E)*** *PCA biplots separated according to support vector machine (SVM) classification on the first three PCs. "Typical" enhancers and promoters where the SVM classification matched the labels are plotted on the left panels, while regions where SVM classification disagreed with labels are plotted on right panels. Contour lines representing the density of enhancer (blue) and promoter (orange) points in the full PCA plot in (D) are overlaid.* ***(F)*** *Heatmaps of CUT&RUN coverage centered on H3K4me1-marked regions from each of the four groups defined in (E). Top to bottom, N = 4,128 typical enhancers, 644 promoter-like enhancers (marked with a red asterisk), 4,707 promoters, and 1,224 enhancer-like promoters.* ***(G)*** *Boxplots summarizing the coverage observed in (F). Boxes are first through third quartiles, center bar median, whiskers extend to 1.5x the interquartile range, outliers are not shown. H3K4me1 was used to select the regions, so differences between groups are expected to be minimal. H3K4me2 through H2BNTac have significant differences each at* $P < 1x10^{-100}$*, and the remaining marks are significant to* $P < 1x10^{-30}$*, by Kruskal-Wallis tests. RPKM = reads per kilobase per million.*

2020) annotated transcription start sites (TSS) – and putative enhancers at least 2 kb from any TSS (Fig 1C, D) (Supp. Table 2).

However, some annotated enhancers cluster with the promoters and vice versa, indicating that these regions have histone modification patterns that resemble the other category (Fig 1E). Inspection of the PCA loadings revealed that H3K4 methylation strongly contributed to the first three principal components (Supp. Fig 1B). Focusing on regions marked by H3K4me1, when visualized in CUT&RUN coverage heatmaps, the "enhancer-like" promoters simply appeared to be inactive compared to the other promoters, with weak acetylation and lacking the classic hallmark of gene activity H3K4me3 (Fig 1F, G, Supp. Fig 1D). By contrast, the "promoter-like" enhancers had comparably strong acetylation to the other enhancers, but were additionally marked by H3K4me2, whereas most enhancers only had H3K4me1 (Fig 1F, G, Supp. Fig 1D). Of note, H3K4me3 was minimal in both enhancer classes (Fig 1F, G, Supp. Fig 1D), consistent with the recent re-evaluation of H3K4 methylation degree at enhancers (Shah et al., 2018). H2BNTac is strongly enriched in typical enhancers but less so in the "promoter-like" enhancers (Fig 1F, G, Supp. Fig 1D), while the core globular acetylation marks H3K56ac, H3K64ac, and H3K122ac, which contribute to subsequent principal components (Supp. Fig 1B), do not distinguish enhancer groups in zebrafish blastulae (Supp. Fig 1E, F). Moving forward, we focused on further characterizing the strong dichotomy of H3Kme2-marked versus non-marked putative enhancers.

H3K4me2-marked distal regions are likely a distinct class of bona fide enhancers

We first considered whether H3K4me2 might not be specific to the promoter-like enhancers at dome stage, but may instead be a temporally variable property of all enhancers. We performed additional CUT&RUN experiments at an earlier and later time point – 1K-cell stage (3 h.p.f.), just prior to the onset of the major wave of genome activation, and shield stage (6 h.p.f.), during gastrulation. We found that H3K4 methylation is overall weak at 1K-cell stage,

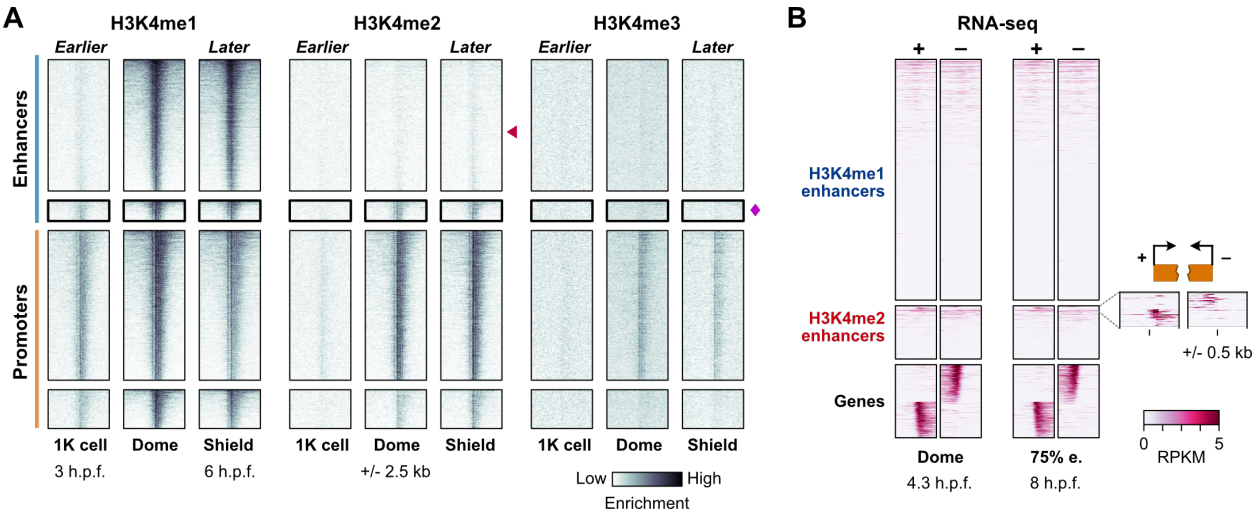

Figure 2. Genomic profiles over time support a stable subset of H3K4me2-marked enhancers. ***(A)*** *Time course of CUT&RUN coverage for the regions defined in Fig 1. Red triangle points to the typical enhancers, which lack H3K4me2 coverage, magenta diamond marks the promoter-like enhancers, which do not gain H3K4me3.* ***(B)*** *Heatmaps of strand-separated RNA-seq coverage centered on the typical enhancers (H3K4me1 enhancers) and promoter-like enhancers (H3K4me2 enhancers), with a subset of gene TSSs shown below to illustrate the expected pattern of unidirectional (-) strand read coverage extending upstream for (-) strand genes and (+) strand coverage extending downstream for (+) strand genes. A zoomed view of coverage at 75% epiboly stage (75% e.) over the top-covered H3K4me2 enhancers is shown to the right. h.p.f. = hours post fertilization, RPKM = reads per kilobase per million.*

with no evidence for H3K4me2 at any putative enhancer, while H3K4me2 presence/absence patterns observed at dome stage are largely preserved at shield stage (Fig 2A, Supp. Fig 2A, B). So, it is unlikely that H3K4me2 is a generic property of all enhancers.

We next considered whether the H3K4me2-marked predicted enhancers (hereafter called H3K4me2 enhancers) may in fact be unannotated gene promoters. H3K4me2 enhancers do not subsequently gain H3K4me3 (Fig 2A, Supp. Fig 2B), nor do they specifically co-occur with repressive marks in previously published datasets for H3K27me3 (Zhang et al., 2014; Zhu et al., 2019), H3K9me3 (Duval et al., 2024), and H2Aub (Hickey et al., 2022) (Supp. Fig 2C), suggesting that these regions are not poised promoters. Additionally, we queried existing RNA-seq datasets (White et al., 2017) looking for evidence of gene-specific transcription but found only ~7% of H3K4me2 enhancers with any evidence for directional, stable transcripts (Fig 2B, Supp. Fig 2D). Although the RNA-seq signal was weak, we removed these regions from subsequent analysis.

To assess the capacity for H3K4me2 enhancers to distally activate gene transcription, we designed and constructed reporter plasmids, cloning 23 putative regulatory elements each upstream of an mCherry open-reading frame with a minimal β-globin promoter (Fig 3A, Supp. Table 3). Independent promoter activity is detected by divergent mTagBFP2 and EGFP open-

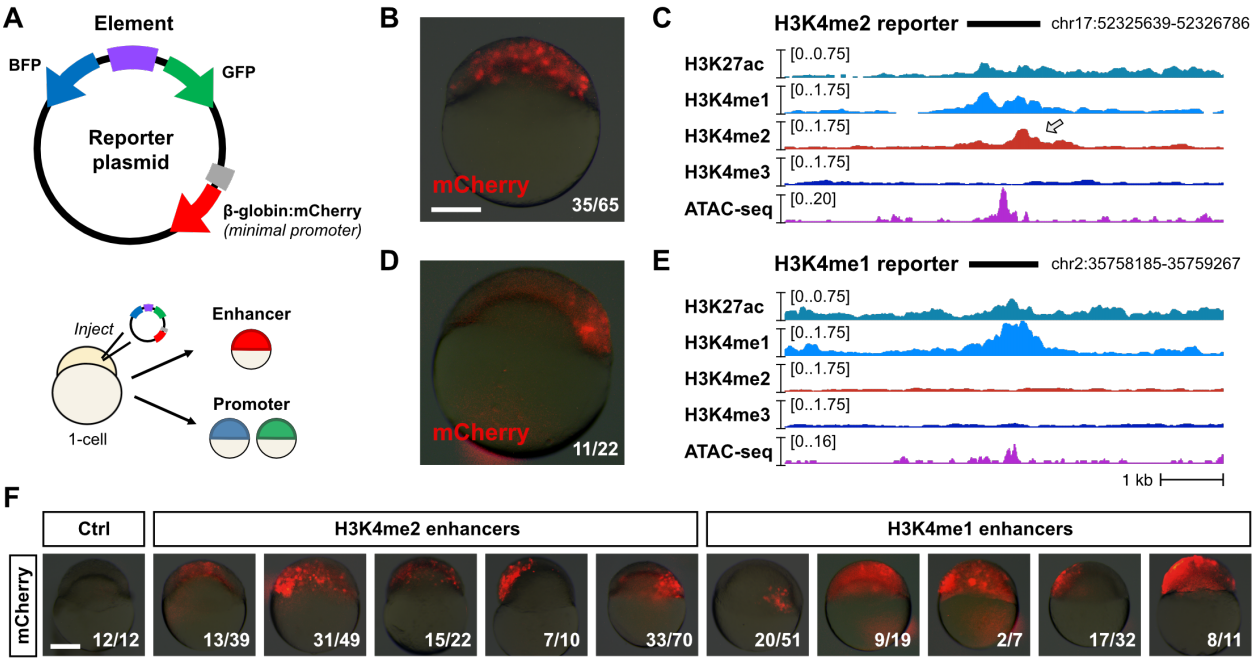

Figure 3. Reporter assays demonstrate enhancer activity. (A) *Map of the reporter plasmid. Putative regulatory elements are cloned in between divergent mTagBFP2 and EGFP open reading frames to detect (-) strand or (+) strand promoter activity as blue or green fluorescence, respectively. Distal regulation is detected by a far downstream mCherry open reading frame with a minimal mouse β-globin promoter. Reporter plasmids are injected into 1-cell embryos and fluorescence is screened in cells (top of the embryo) in the late blastula / early gastrula.* ***(B)*** *mCherry fluorescence from a reporter (Enh_2a) encoding a putative H3K4me2 enhancer. A brightfield image at 25% opacity is overlaid. Fraction of injected embryos fluorescing is shown on the bottom right.* ***(C)*** *Genome browser tracks showing CUT&RUN (this study) and ATAC-seq open fragment coverage (data from Liu et al, 2018) over the H3K4me2 reporter tested in (B) (black bar). Arrow points to the H3K4me2 enrichment.* ***(D)*** *mCherry fluorescence for an H3K4me1 reporter (Enh_1a).* ***(E)*** *Genome browser track for the reporter tested in (D).* ***(F)*** *mCherry fluorescence for five additional H3K4me2 (Enh_2b-f, middle group) and H3K4me1 enhancers (Enh_1b-f, right group). Control embryos injected with empty reporter plasmids have no fluorescence (left panel). Scale bar = 250 μm.*

reading frames (Fig 3A, Supp. Fig 3A). We performed transient expression assays by injecting plasmid into 1-cell embryos and visualizing fluorescence at 6 h.p.f. to allow time for fluorophore transcription, translation, and maturation. Ten H3K4me2 enhancers and 10 H3K4me1 enhancers drove mosaic mCherry expression (likely due to injection variability) of varying intensity, demonstrating their enhancer capability (Fig 3B-F, Supp. Fig 3A-C). We additionally observed some mostly weak GFP or BFP expression for three H3K4me2 and three H3K4me1 reporters, suggesting some dual enhancer-promoter functionality (Supp. Fig 3, Supp. Table 3). All together, these results support the existence of two distinct enhancer classes in the early embryo with similar regulatory capacity to drive gene activation during the MZT.

H3K4me2 enhancers are activated by maternal mechanisms independent of known pioneer factors

We next sought to understand how H3K4me2 enhancers become active during the MZT.

First, to determine whether enhancers gain H3K4 methylation through maternal or zygotic mechanisms, we inhibited genome activation by treating embryos with the Pol II transcription elongation inhibitor triptolide (Chan et al., 2019; Kontur et al., 2020) and performed CUT&RUN for H3K4me1 and H3K4me2, including a yeast mononucleosome spike-in to aid in normalization (Fig 4A, Supp. Fig 4A). We found that triptolide-treated embryos maintain the pattern of H3K4me1 and H3K4me2 marks observed in DMSO-treated control embryos, again clearly distinguishing the two enhancer classes. Thus, enhancer H3K4 methylation occurs through maternal mechanisms, suggesting that H3K4me2 enhancers can participate in zygotic genome activation.

Next, we asked whether maternal NPS pluripotency factors equivalently regulate both enhancer classes. We analyzed previously published blastula ChIP-seq data for Nanog, Pou5f3, and Sox19b (Miao et al., 2022; Xu et al., 2012) and found widespread binding across both H3K4me1 and H3K4me2 enhancers, though with somewhat less intensity for the latter (Fig 4B). When we inspected the underlying sequence for the binding motifs recognized by the factors, we found that H3K4me2 enhancers were significantly depleted for these motifs compared to the H3K4me1 enhancers ($P < 1 \times 10^{-11}$, Chi-squared tests, 2 d.o.f.) (Fig 4B, Supp. Fig 4B), suggesting that NPS may not be binding directly or specifically to many of the H3K4me2 enhancers.

In MZ*nps* mutants, the absence of the three maternal pluripotency factors leads to loss of chromatin accessibility and H3K27ac across many enhancers (Miao et al., 2022). When we compared sphere-stage ATAC-seq open chromatin and H3K27ac ChIP-seq coverage between wild-type and MZ*nps*, we found that H3K4me2 enhancers indeed do not require NPS for their accessibility or H3K27ac acquisition, in stark contrast to the H3K4me1 enhancers (Fig 4C). Together, these data demonstrate that H3K4me2 enhancers are largely NPS-independent.

We considered the possibility that H3K4me2 enhancers may be activated by a yet-unknown maternal transcription factor. However, ChIP-seq binding profiles of other putative maternal activators (Dubrulle et al., 2015; Ladam et al., 2018; Miao et al., 2022; Stanney et al., 2020) showed no strong enrichment at H3K4me2 enhancers over H3K4me1 enhancers (Supp. Fig 4C). Motif enrichment analysis revealed some transcription factor binding sequences, but none that unify the H3K4me2 enhancers compared to the H3K4me1 enhancers (Supp. Fig 4D). Thus, NPS pioneering underlies H3K4me1 enhancer activation, but H3K4me2 enhancers as a group seem to activate independent of NPS or any other known sequence-specific pioneer factor.

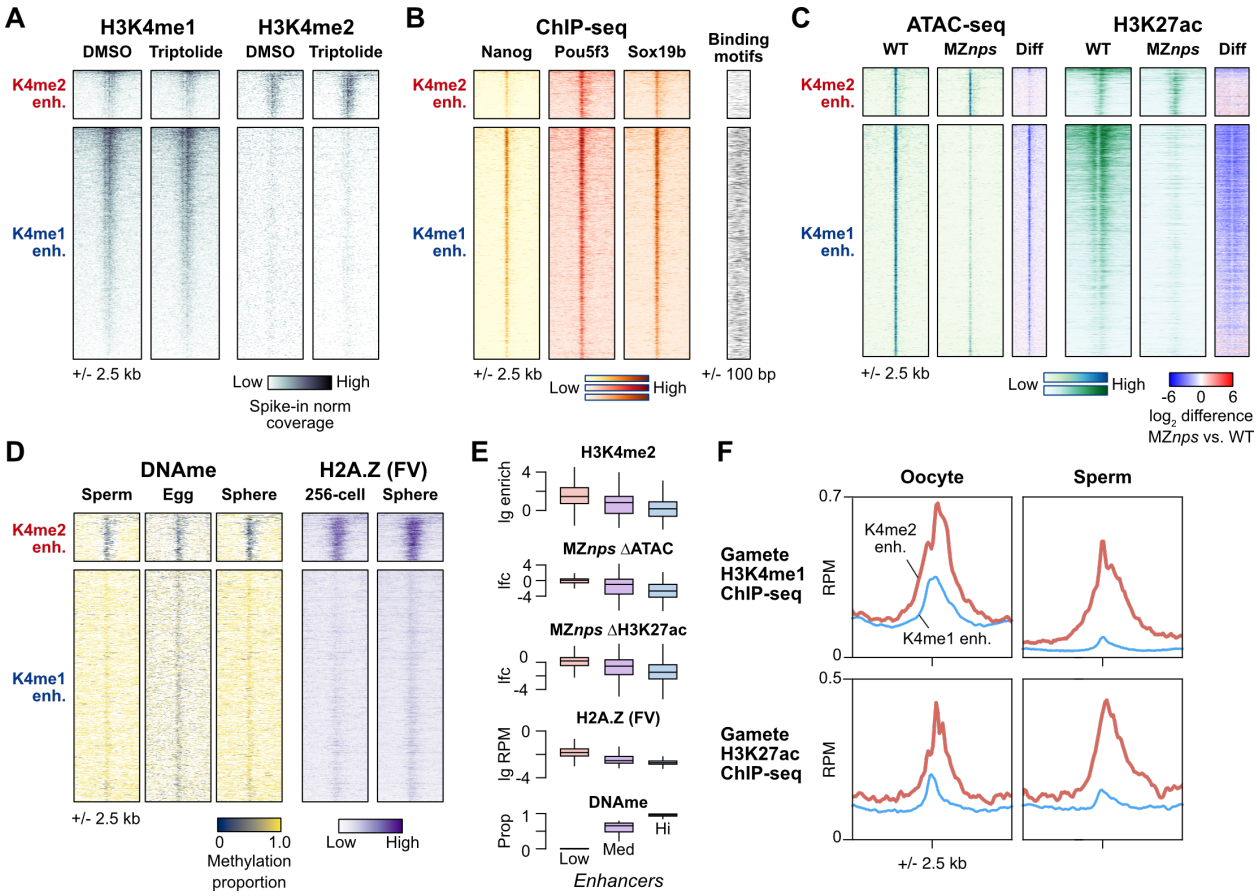

Figure 4. H3K4me2 enhancers have distinct activation pathways. (A) *Heatmaps over H3K4me2-marked enhancers (K4me2 enh.) and non H3K4me2-marked enhancers (K4me1 enh.) showing H3K4me1 and H3K4me2 CUT&RUN coverage in control DMSO embryos and embryos treated with the Pol II inhibitor triptolide.* ***(B)*** *ChIP-seq coverage for Nanog, Pou5f3, and Sox19b (data from Miao et al, 2022). Binding motif occurrence for the three factors over the regions is represented as a heatmap on the right.* ***(C)*** *ATAC-seq open fragment and H3K27ac ChIP-seq coverage in wild-type embryos and MZnps embryos (data from Miao et al, 2022). Log_2-fold difference heatmaps of MZnps coverage versus wild-type are shown on the right for each chromatin feature.* ***(D)*** *DNA methylation proportion from bisulfite sequencing (data from Potok et al, 2013) and H2A.FV ChIP-seq coverage (data from Murphy et al, 2018).* ***(E)*** *Boxplots comparing correlated chromatin features on enhancers separated into groups with low (<20%), medium (20-80%), and high (>80%) DNA methylation. Boxes are first through third quartiles, center bar median, whiskers extend to 1.5x the interquartile range, outliers are not shown.* ***(F)*** *Aggregate plots for the two embryonic enhancer groups (K4me2 enhancers, thick red curves; K4me1 enhancers, thin blue curves) showing oocyte and sperm H3K4me1 ChIP-seq average coverage (data from Zhang et al, 2018, and Murphy et al, 2018, respectively) and oocyte and sperm H3K27ac (data from Zhang et al, 2018). lg = log_2, lfc = log_2 fold change, RPM = reads per million.*

H3K4me2 enhancers are hypomethylated and enriched for H2A.Z

In the absence of strong evidence for a novel pioneer factor, we looked instead for epigenetic differences between the two enhancer classes. Previously, Kaaji et al found that putative zebrafish embryonic enhancers exhibit a range of DNA methylation levels, which was also correlated with different chromatin characteristics including H3K4 methylation degree (Kaaij et al., 2016), while Murphy et al demonstrated that a subset of hypomethylated embryonic promoters gain accessibility through H2A.Z-containing placeholder nucleosomes (Murphy et al.,

2018). Given that we originally identified H3K4me2 enhancers due to their similarity to promoters, we queried previously published bisulfite sequencing (Potok et al., 2013) and H2A.Z (H2AFV) ChIP-seq data (Murphy et al., 2018). We indeed found that H3K4me2 enhancers are strongly hypomethylated in the egg and maintain low DNA methylation through genome activation (Fig 4D, E, Supp. Fig 4E, F), in contrast to H3K4me1 enhancers, which are hypermethylated. Additionally, H3K4me2 enhancers but not H3K4me1 enhancers acquire strong H2A.FV levels (Fig 4 D,E). Thus, H3K4me2, lack of NPS dependence, low DNA methylation, and H2A.Z are all correlated chromatin features that distinguish a subset of zebrafish embryonic enhancers (Fig 4E)

Genome-wide, DNA methylation patterns in the zebrafish embryo have been found to be reprogrammed to match sperm and not the oocyte/egg (Jiang et al., 2013; Potok et al., 2013), and indeed we find that here to generally be the case for embryonic enhancers (Fig 4D, Supp. Fig 4G). However, a large fraction (69%) of hypomethylated embryonic enhancers is equivalently hypomethylated in both eggs and sperm (Supp. Fig 4G, H), suggesting that these represent a shared enhancer set used by both gametes and embryos. Indeed, querying existing gamete H3K4me1 and H3K27ac ChIP-seq data (Murphy et al., 2018; Zhang et al., 2018) reveals that the embryonic H3K4me2 enhancers identified here have high levels of these activating histone marks in both oocytes and sperm, while H3K4me1 enhancers do not (Fig 4F, Supp. Fig 4I). Thus, H3K4me1 and H3K4me2 enhancers' orthogonal activation pathways may relate to their past activity in gametes: the former rely on maternal factor pioneering to establish de novo activity, while the latter already have a history of activity in gametes and are epigenetically bookmarked to resume activity in the embryo.

H3K4me2 enhancers likely activate NPS-independent genes

Given that H3K4me2 enhancers are activated through non-NPS dependent pathways, we asked whether they could underlie activation of genes not repressed in MZ*nps* embryos. It is likely that each zygotic gene is regulated by multiple enhancers with variable levels of redundancy, additivity, or synergy that contribute to expression levels, which would complicate deducing regulatory dependence (Kvon et al., 2021). Despite this, under a strict definition (>3-fold enriched H3K4me2 CUT&RUN signal over IgG), we find that H3K4me2 enhancers are mildly but significantly nearer to non NPS-dependent gene promoters compared to H3K4me1 enhancers ($P = 3.3x10^{-6}$, Wilcoxon rank sum test), indicating a potential regulatory relationship (Fig 5A). This is not the case for NPS-dependent genes ($P = 0.06$, Wilcoxon rank sum test) (Fig 5A). But reversing the perspective, NPS-dependent and non-NPS dependent genes seem to

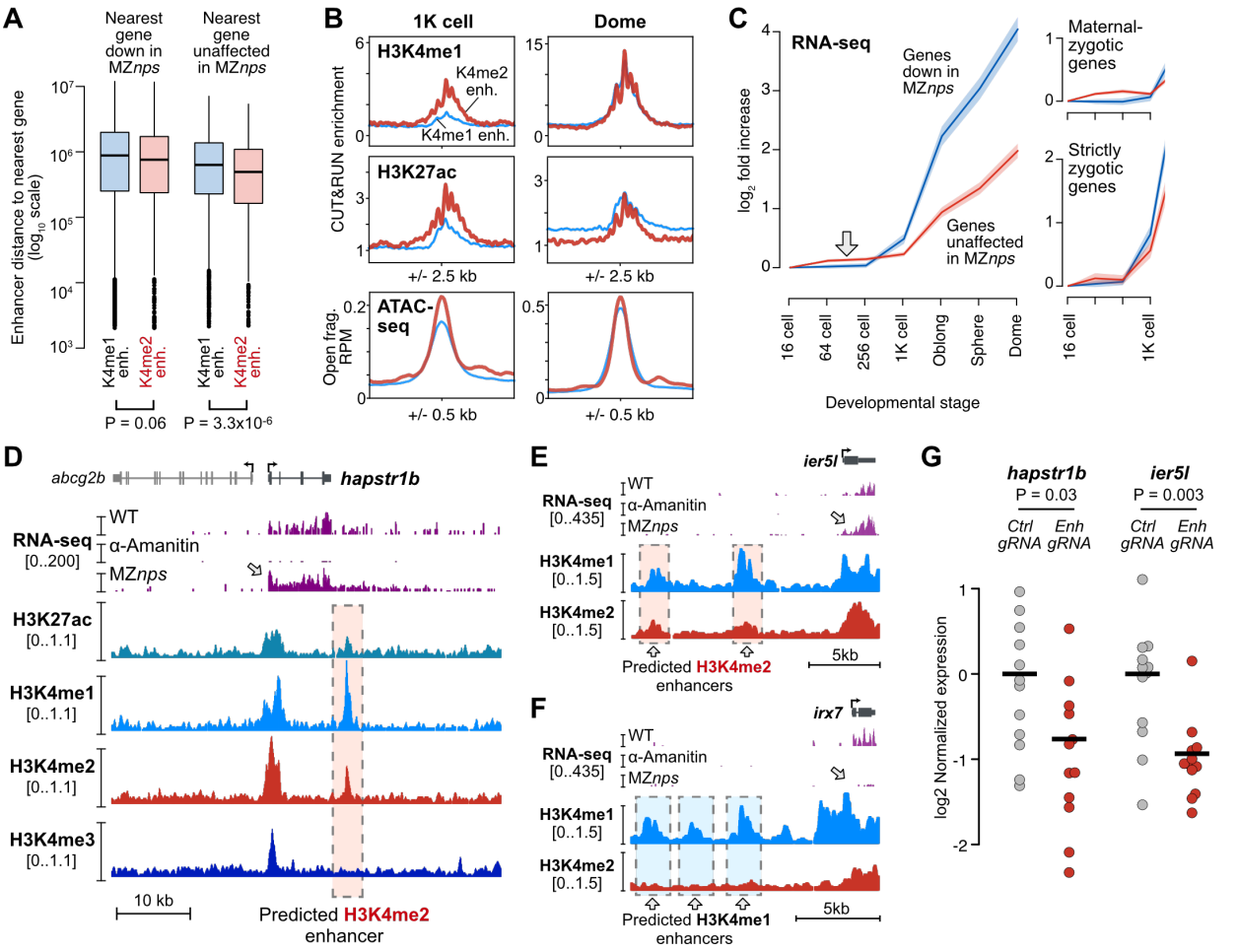

Figure 5. H3K4me2 enhancers likely regulate non NPS-dependent genes. (A) *Boxplots representing the distance to the nearest gene for each enhancer, for each enhancer/gene combination. Boxes are first through third quartiles, center bar median, whiskers extend to 1.5x the interquartile range, points are outliers.* ***(B)*** *Aggregate plots of CUT&RUN (this study) and ATAC-seq open fragment coverage (data from Liu et al, 2018). K4me2 enhancer average plotted as thick red curves, K4me1 enhancer average as thin blue curves.* ***(C)*** *Plot of average wild-type RNA-seq log_2 fold increase over time for genes according to their fate in MZnps embryos – down in MZnps as classified by Miao et al, 2022 (blue line) or unaffected (red line). 95% confidence intervals are highlighted. Right panels show the plot stratified into genes with a maternal contribution (maternal-zygotic) or strictly zygotic genes. RNA-seq data from Vejnar et al, 2019.* ***(D-F)*** *Genome browser tracks illustrating regions with predicted enhancers. Top tracks show Click-iT RNA-seq coverage in wild-type, α-amanitin treated, and MZnps embryos (data from Miao et al, 2022). Lower tracks show CUT&RUN coverage (this study). Predicted enhancers are highlighted with dashed boxes.* ***(G)*** *qRT-PCR quantification of zygotic gene expression (hapstr1b or ier5l) in individual F0 CRISPR-Cas9 enhancer loss-of-function embryos targeting the predicted hapstr1b enhancer shown in (D) (left) and two ier5l enhancers simultaneously, shown in (E) (right).*

have equivalent potential to be regulated by both H3K4me1 and H3K4me2 enhancers, with >95% of genes from either group potentially residing within 1 Mb of either class of enhancers (Supp. Fig 5A-C). This likely reflects the regulatory complexity of promoter-enhancer relationships, especially given that NPS-dependent genes show varying levels of residual activation even in the absence of NPS (Miao et al., 2022).

We did however find evidence for a functional connection between H3K4me2 enhancers and non NPS-dependent genes. There is a temporal asymmetry in the activation of the two enhancer classes that is mirrored by the expression dynamics of differentially NPS-dependent genes. At 1K-cell stage, we detect higher levels of H3K4me1, H3K27ac, and chromatin accessibility in H3K4me2 enhancers compared to H3K4me1 enhancers (Fig 2A, Fig 5B, Supp. Fig 2A), demonstrating that H3K4me2 enhancers are activated earlier. By dome stage, the signals equalize (Fig 5B, right). We note that H3K4 methylation levels are overall low at 1K-cell stage and barely detectable at enhancers only when using an alternate H3K4me1 antibody (Supp. Fig 2A). Concomitantly, we find that across several RNA-seq time courses, non NPS-dependent genes have earlier detectable up-expression than NPS-dependent genes by at least two cell cycles (Fig 5C, Supp. Fig 5D-G), though NPS-dependent genes subsequently overtake non NPS-dependent genes in magnitude of increase. This phenomenon is unlikely due to dynamic poly(A) tail lengths because we observe the trend in ribosomal RNA-depleted, spike-in normalized datasets (Fig 5C, Supp. Fig 5D) as well as with 4SU metabolic labeling of de novo transcription (Supp. Fig 5F). The effect seems to be primarily driven by maternal-zygotic gene activation (Fig 5C, right, Supp. Fig 5D), consistent with our model where H3K4me2 enhancers are recapitulating oocyte roles during the MZT, reactivating some of the same genes that previously helped shape the maternal contribution (Fig 4F, Supp. Fig 4I).

H3K4me2 enhancer loss of function reduces activation of NPS-independent genes

Finally, we used an F0 CRISPR-Cas9 strategy to target specific H3K4me2 enhancers likely regulating non NPS-dependent zygotic genes (Fig 5D-F). We injected 1-cell embryos with Cas9 protein complexed with a pool of three different guide RNAs targeting a predicted H3K4me2 enhancer downstream of non NPS-dependent *hapstr1b* (Fig 5D, Supp. Fig 6A). We measured *hapstr1b* activation in individual crispant embryos at sphere stage by quantitative reverse-transcription PCR (qRT-PCR) and found on average a 1.7-fold decrease in *hapstr1b* expression compared to control embryos injected with Cas9 + guide RNAs targeting the non-zygotic *slc45a2* (*albino*) promoter ($P = 0.03$, Wilcoxon rank sum test) (Fig 5G). The downregulation is highly variable, as is expected from embryo-to-embryo variability in Cas9 targeting efficacy. As we could not recover sufficient genomic DNA from embryos at such an early developmental stage for genotyping, we instead genotyped sibling crispants at 32 h.p.f. by PCR. We indeed found mosaic patterns of genomic lesions in the *hapstr1b* enhancer locus (Supp. Fig 6A, B), which likely underlie variable effects on *hapstr1b* activation.

We additionally tested two predicted H3K4me2 enhancers upstream non NPS-dependent *ier5l* (Fig 5E, Supp. Fig 3B, Supp. Fig 6C), which were not included in our earlier analyses due to lower H3K27ac enrichment at dome stage. Nonetheless, when we targeted both enhancers in parallel with CRISPR-Cas9 and two guide RNAs per enhancer, we found an average 1.9-fold decrease in *ier5l* expression in F0 crispants compared to *albino* controls ($P = 0.003$, Wilcoxon rank sum test) (Fig 5G). Crispant siblings similarly exhibited mosaic genomic lesions (Supp. Fig 6C-E). Thus, H3K4me2-marked enhancers can regulate zygotic expression of genes that do not depend on maternal NPS pioneer factors.

Discussion

Here, we have demonstrated that two distinct sets of enhancers regulate the maternal-to-zygotic transition in zebrafish, contributing to widespread gene activation as the embryo induces pluripotent stem cells. Among the 10 histone modifications we profiled using CUT&RUN, it is only H3K4 methylation degree that strongly distinguishes these two enhancer classes. H3K4me3 is not enriched at any enhancer. Putative enhancers marked by H3K4me1 but not H3K4me2 attain chromatin accessibility and activating histone modifications de novo in the embryo through the pioneering activities of maternal pluripotency factors Nanog, Pou5f3, and Sox19b. In contrast, enhancers marked by H3K4me2 are hypomethylated early, which facilitates acquisition of H2A.Z-bearing nucleosomes that promote open chromatin independent of maternal NPS. A large proportion of these H3K4me2 enhancers overlap with putative hypomethylated oocyte enhancers, suggesting that H3K4me2 enhancers recapitulate gamete regulatory activities in the embryo. Thus, parallel enhancer activation pathways operate during the maternal-to-zygotic transition that are responsible for activating different zygotic gene repertoires (Fig 6).

A unified model of zygotic genome activation

Our findings unite and extend several previous studies aiming to decipher the regulatory logic of zebrafish embryonic genome activation. The initial discovery that maternally provided pluripotency factors Nanog, Pou5f3, and Sox19b play major roles in genome activation (M. T. Lee et al., 2013; Leichsenring et al., 2013) reinforced the regulatory connection between transcriptional reprogramming during the maternal-to-zygotic transition in non-mammalian vertebrates and pluripotency induction in mammalian cells. However, these factors did not account for all zygotic gene activation, implicating additional unknown mechanisms. Subsequent elucidation of NPS's pioneering activity at many but not all promoters and enhancers motivated

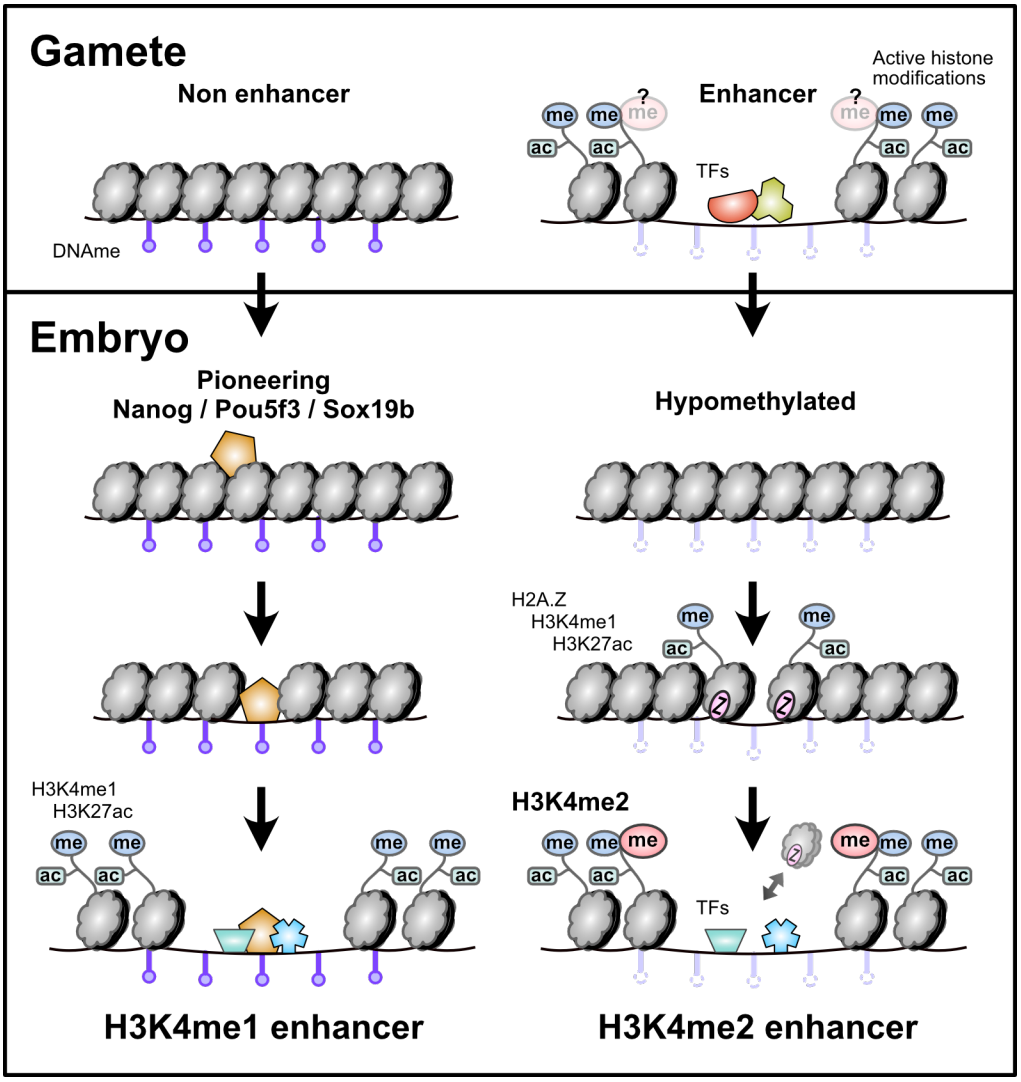

Figure 6. Parallel enhancer activation pathways during the maternal-to-zygotic transition. *Enhancers that lack evidence for gamete activity are hypermethylated, rely on NPS-pioneering, and are marked with H3K4me1 but not H3K4me2 in the embryo. Enhancers that have evidence for gamete activity are hypomethylated, recruit H2A.Z-containing placeholder nucleosomes rather than relying on NPS pioneering, and are marked with H3K4me2.*

the search for additional factors that could similarly engage and activate nascent, condensed embryonic chromatin (Liu et al., 2018; Miao et al., 2022; Pálfy et al., 2019; Veil et al., 2019).

Meanwhile, several groups recognized the role of DNA methylation in influencing early embryonic regulatory sequence activity (Hickey et al., 2022; Jiang et al., 2013; Kaaij et al., 2016; Lee et al., 2015; Liu et al., 2018; Murphy et al., 2018; Potok et al., 2013; Wu et al., 2021; Zhang et al., 2018). Hypomethylation was found to be associated with open chromatin at promoters (Liu et al., 2018; Zhang et al., 2018), and the characterization of embryonic H3K4me1/H2A.Z-bearing placeholder nucleosomes by Murphy et al provided a mechanism for the acquisition and maintenance of promoter accessibility (Murphy et al., 2018). By contrast,

enhancers overall were found to be hypermethylated, which was surprising given the correlation between high DNA methylation and gene repression described in other systems (Kaaij et al., 2016; Lee et al., 2015; Liu et al., 2018; Zhang et al., 2018). Zhang et al noted that these enhancers were distinct from gamete enhancers (Zhang et al., 2018), and Liu et al hypothesized that NPS were uniquely capable of binding methylated DNA in the embryo (Liu et al., 2018). Kaaij et al recognized that some distal loci were instead hypomethylated, while also bearing bivalent repressive H3K27me3 and activating H3K4me2 and H3K4me3 (Kaaij et al., 2016) (though, antibody specificity may have been confounding, see (Shah et al., 2018)), suggesting that these represented poised enhancers that would later play cell-type-specific roles. Hickey et al subsequently showed that acquisition of repressive H2Aub and later H3K27me3 at hypomethylated enhancers also depended on placeholder nucleosome acquisition (Hickey et al., 2022). Finally, Wu et al found that inhibiting DNA methylation led to ectopic enhancer activation and acquisition of H3K4me3 (contingent on antibody specificity), further linking hypomethylation with higher order H3K4 methylation (Wu et al., 2021).

We now find that a subset of hypomethylated enhancers shared with gametes are indeed active in the early embryo and uniquely acquire H3K4me2. These H3K4me2 enhancers likely account for non NPS-dependent embryonic gene activation during the maternal-to-zygotic transition, while enhancers bearing only H3K4me1 correspond to NPS-pioneered enhancers that regulate NPS-dependent genes. This division of labor has implications for how proper transcriptome composition and cellular identity may be maintained throughout germ cell and embryonic development. The maternal contribution is transcribed and curated during the germ cell-to-maternal transition (Abrams and Mullins, 2009; Blatt et al., 2021) to contain the potent reprogramming cocktail centered around Nanog, Pou5f3, and Sox19b, which will eventually induce genome activation and pluripotency in the embryo. Until then, NPS activity presumably must be inhibited to prevent ectopic transcription of developmental triggers. This can be accomplished by limiting their translation until after egg activation (Lorenzo-Orts and Pauli, 2024), but also by inhibiting their target enhancers in the oocyte through DNA methylation. It is still unknown why NPS can activate methylated DNA in the zebrafish embryo, but the high concentration of these factors that accumulates through extremely elevated translation (M. T. Lee et al., 2013) may contribute to their pioneering capacity (Hansen and Cohen, 2022; Yan et al., 2018). Conversely, oocyte enhancers that supported transcription of the maternal contribution would not need to be so tightly controlled, since any aberrant activity would simply add to the existing maternal mRNA pool, allowing them to remain poised through hypomethylation to be reactivated in the embryo.

Clarifying H3K4 methylation degree at enhancers

H3K4 methylation has long been recognized as a hallmark of enhancer loci, and the predominance of H3K4 mono-methylation specifically distinguished enhancers from gene-proximal regions that tend to bear di- and tri-methylation (Barski et al., 2007; Ernst et al., 2011; Heintzman et al., 2007; Wang and Helin, 2024; Zentner et al., 2011). Some reports have suggested that enhancers can indeed attain H3K4me3 (Hu et al., 2017; Koch and Andrau, 2011; Liu et al., 2024; Pekowska et al., 2011), somewhat blurring the distinction between enhancers and promoters. However, these conclusions are called into question by the recent finding that H3K4 methyl antibody cross-reactivity may contribute to false detection of higher-degree methylation at many loci. Using rigorously tested antibodies, Shah et al demonstrated that at least in K562 cells, only H3K4me1 and H3K4me2 but not H3K4me3 are characteristic of enhancers (Shah et al., 2018). Here, we extend these results to zebrafish blastulae: indeed, H3K4me3 is not enriched at enhancers, but we also find that H3K4me2 is not a generic property of all enhancers, but rather marks only a subset of hypomethylated, putative gamete-inherited enhancers that do not depend on pluripotency factor pioneering.

Our findings are reminiscent of a recent report that H3K4me3 marks a putative TCF enhancers in mouse oocytes as well as a subset of enhancers in pre-implantation embryos, during a period of global DNA demethylation (Liu et al., 2024). These enhancers are likely not related to the zebrafish H3K4me2 enhancers, which do not have evidence for TCF binding (Supp. Fig 4D); and moreover, mammalian ZGA is in many ways mechanistically distinct from zebrafish genome activation (Guo et al., 2024; Lee et al., 2014; Svoboda, 2018; Vastenhouw et al., 2019). Regardless, together with our findings, this suggests that some higher-order H3K4 methylation at enhancers may be correlated with the transmission of epigenetic information from the germline to the embryo, or during cellular transitions generally, distinguishing persistent or “reawakened” enhancers from “reprogrammed” enhancers that are newly activated. The extent to which this distinction exists in other contexts, e.g. embryonic or artificial pluripotency induction in mammals, remains to be determined.

Additional regulatory players remain to be elucidated

How precise H3K4 methylation degree is achieved at the two enhancer classes likely involves differential recruitment of chromatin regulators, particularly methyltransferases. Vertebrates encode six major H3K4 methyltransferase variants (Van et al., 2024), many of which are duplicated in zebrafish. In vitro, KMT2A/B (MLL1/2) and KMT2F/G (SETD1A/B) are

capable of catalyzing all three of mono-, di-, and trimethylation, while KMT2C/D (MLL3/4) can only catalyze mono- and dimethylation (Li et al., 2022). However, the kinetics suggest that KMT2A/B and KMT2C/D preferentially generate H3K4me2 and H3K4me1, respectively (Li et al., 2022). KMT2C/D have been shown to install H3K4me1 at enhancers (Herz et al., 2012; Hu et al., 2013; Jozwik et al., 2016; J.-E. Lee et al., 2013; Wang et al., 2016), though KMT2A/B have also been found to localize to some enhancers (Hu et al., 2017; Zhang et al., 2016). Concordantly, zebrafish H3K4me1 and H3K4me2 enhancers could arise through differential recruitment of these methyltransferases, via mechanisms specific to their respective activation pathways. KMT2A/B contains CXXC domains that direct it to specifically unmethylated CpGs (Allen et al., 2006; Ayton et al., 2004; Birke et al., 2002), which could underlie how hypomethylated enhancers attain H3K4me2. Indeed, Liu et al showed a link between hypomethylated promoter accessibility and Kmt2a and Cxxc1b, the zebrafish ortholog of CXXC1 (CFP1) that complexes with KMT2F/G to similarly target unmethylated CpGs (Lee and Skalnik, 2005; Liu et al., 2018).

We presume that specific maternal transcription factors engage each enhancer and contribute to the recruitment of chromatin factors (Chan et al., 2019; Miao et al., 2022). Unlike the NPS-bound H3K4me1 enhancers, H3K4me2 enhancers as a group do not have strong enrichment for any one binding motif (Supp. Fig 4D), suggesting that a diverse collection of factors each bind a subset of different enhancers. This could account for the dozens of other transcription factors represented in the maternal contribution (M. T. Lee et al., 2013), which likely have combinatorial roles across both enhancer classes in elaborating individual gene expression levels. This is likely true for all enhancers, but it is only a requirement for NPS pioneering that underlies the strong NPS motif signature in H3K4me1 enhancers, a function that is unnecessary for H3K4me2 enhancers. Though, we cannot ignore the transcriptional activating functions of NPS, and indeed at the peak of genome activation, their zygotic gene targets do seem to be more strongly activated on average than non-NPS targets (Fig 5C, Supp. Fig C-F).

Finally, the regulatory logic underlying DNA methylation reprogramming is still incompletely understood. This is particularly relevant for the subset of hypomethylated embryonic enhancers that were previously hypermethylated in the oocyte (Supp. Fig 4G, H), suggesting that some enhancers may interconvert between activation pathways. Further characterization of the underlying chromatin is warranted as we continue to dissect the regulatory logic of the maternal-to-zygotic transition and embryonic pluripotency induction.

Methods

Animal Husbandry

All animal procedures were conducted under the supervision and approval of the Institutional Animal Care and Use Committee at the University of Pittsburgh, Protocol #21120500. *Danio rerio* were housed in a recirculating aquatic system (Aquaneering) at 28ºC with a 14/10 hour light/dark cycle (light 8 a.m. to 10 p.m.). Fish were fed 2x daily (10 a.m. and 2 p.m.) with Artemia nauplii.

Embryo collection

Four to five adult TUAB males and females each were set in divided 1.7 L sloped breeding tanks (Tecniplast #ZB17BTE) overnight. Water was changed and dividers removed at 8-9 a.m. the following morning, and embryos were collected at 1-cell stage. Embryos were dechorionated by treatment with 1 mg/mL Pronase (Sigma #P5147) in egg water (60 µg/mL ocean salt in DI water) for two minutes then washed. Embryos were incubated at 28.5ºC on agarose coated petri dishes with egg water and collected at appropriate stages as determined by morphology.

For Triptolide (Apexbio #MFCD00210565) treatment, a 4 mM stock solution dissolved in DMSO was added to 1-cell stage embryos in 6-well plates to a final concentration of 2 µM Triptolide and 0.05% DMSO in egg water. DMSO control wells were treated with 0.05% DMSO final. Embryos were collected when DMSO control embryos reached dome stage.

CUT&RUN

The CUT&RUN procedure was adapted from Hainer et al (Hainer et al., 2019), which incorporates optimizations of the method of Skene and Henikoff (Skene and Henikoff, 2017). For each sample, approximately 70,000 cells were used: 70 1K-cell stage, 10 dome stage, or 8 shield stage embryos, using average stage cell counts from (Joseph et al., 2017). Embryos were deyolked in batches of 50-200 embryos: embryos were transferred to 1.5 mL Eppendorf tubes removing excess liquid with a P200 pipettor, then yolk lysis buffer added (55 mM NaCl,1.8 mM KCl, 1.25 mM NaHCO3). Tubes were shaken at 1100 RPM for 5 min at room temperature, centrifuged at 300xg for 30 sec to pellet, yolk lysis buffer drawn off, and 1 mL Yolk Lysis Wash Buffer was added (110 mM NaCl, 3.5 mM KCl, 2.7 mM CaCl2, 10 mM Tris pH 8.5). Tubes were shaken at 1100 RPM for 2 minutes at RT, centrifuged at 300xg to pellet, and supernatant was again removed and replaced with 600 µL Nuclear Extraction Buffer (20 mM HEPES-KOH, pH 7.9, 10 mM KCl, 500 µM spermidine, 0.1% Triton X-100, 20% glycerol).

Samples in Nuclear Extraction Buffer were gently resuspended by pipetting up and down, centrifuged at 600xg at 4ºC for 3 min, supernatant removed, and again resuspended in 600 µL Nuclear Extraction Buffer. To bind nuclei, 150 µL of concanavalin A beads (Polysciences #86057) per sample were activated by added to 850 µL Binding Buffer (20 mM HEPES-KOH pH 7.9, 10 mM KCl, 1mM $CaCl_2$, 1mM $MnCl_2$), placed on a magnet stand, and washed twice with Binding Buffer. Beads were resuspended in 300 µL Binding Buffer and slowly added to nuclei with gentle vortexing (~1500 rpm), then rotated 10 min at RT. Supernatant was drawn off on a magnet stand, then beads were blocked for 5 min in 1 mL Wash Buffer (20 mM HEPES-KOH pH 7.5, 150 mM NaCl, 0.5 mM spermidine, 0.1% BSA w/v) with 2mM EDTA for 5 min at RT. To bind antibody, supernatant was drawn off on a magnet stand and washed 2x with 1 mL Wash Buffer. Beads were resuspended in 500 µL of 1:100 primary antibody in Wash Buffer for 2 hr at 4ºC on a rotator. To bind pAG-MNase, beads were washed 2x in 1 mL Wash Buffer, then resuspended in 500 µL of 1:200 pAG-MNase (gift from Sarah Hainer) in Wash Buffer for 1 hr at 4ºC, and washed again 2x with Wash Buffer. Beads were resuspended in 150 µL Wash Buffer and placed on ice for 5 min, then the pAG-MNase was activated by adding 3 µL 100 mM $CaCl_2$ while gentle vortexing and returning to ice. After 30 min, the reaction was stopped using 2x STOP Buffer (200 mM NaCl, 20 mM EDTA, 4 mM EGTA, 50 µg/mL RNase A, 40 µg/mL glycogen; and 10 pg/mL yeast mononucleosome as a spike-in (20 pg/mL for the Triptolide experiments). Nuclei were incubated at 37ºC for 20 min followed by centrifuging for 5 min at 16,000xg at 4ºC, drawing off the DNA fragments with the supernatant. The extracted fragments were treated with SDS (0.1%) and proteinase K (2.5 µL of 20 mg/mL stock) at 70ºC for 10 min followed by phenol chloroform extraction and ethanol precipitation. Purified DNA was resuspended in 50 µL of water. Antibodies used were: H3K4me1, Invitrogen #710795, lot #2477086 (all stages), and ActiveMotif #39297, lot #01518002 (for 1K-cell stage only); H3K4me2, Invitrogen #710796, lot #2246656; H3K4me3, Invitrogen #711958, lot #2253580; H3K27ac, Abcam #ab4729, lot #GR3357415-1; H3K9ac, Cell Signaling #9649, lot #13; H3K56ac, Invitrogen #PA5-40101, lot #XA3485152A; H3K64ac, Abcam #ab214808, lot #GR3312057-4; H3K122ac, Abcam #ab33309, lot #GR3427528-1; H4K16ac, Millipore #37707329, lot #3770263; H2BK16ac, Abcam #ab177427, lot #GR199432-1; IgG, Invitrogen #10500C. CUT&RUN libraries were constructed using the NEB Ultra II DNA library prep kit (NEB #E7645) and indexed adapters according to manufacturer's protocol. DNA was end repaired and then ligated to sequencing adaptors diluted 1:100. Ligated DNA was purified with 0.9x Sera-Mag Select beads (Cytiva #29343045) and PCR amplified for 15 cycles, then purified again with 0.9x Sera-Mag beads. Libraries were run on a 1.5% TBE agarose gel, and a band

corresponding to 175 - 650 bp was cut out and gel purified using the NEB Monarch DNA gel extraction kit (#T1020). Concentration was verified by Qubit dsDNA high sensitivity and Fragment Analyzer. Sequencing libraries were multiplexed and paired-end sequenced on an Illumina NextSeq 500 at the Health Sciences Sequencing Core at Children's Hospital of Pittsburgh.

In Vivo Reporter Assay

For the enhancer reporter plasmid, starting with a pTol2 α-crystallin mCherry plasmid, CMV:EGFP was amplified from pCS2+ cytoplasmic EGFP (gift from Antonio Giraldez) using F-aaactagagattcttgtttagaattcGTCGACCATAGCCAATTCAATATGGC and R-ctagagtcgaGGTACCGGGCCCAATGCA and inserted using NEB HiFi Assembly (NEB #E5520). The β-globin minimal promoter was amplified from mouse genomic DNA (gift from Sarah Hainer) using F-aaaggtaCCAATCTGCTCAGAGAGGACA, R-aaagctagcGATGTCTGTTTCTGAGGTTGCA and cloned into the plasmid with KpnI/NheI to replace the existing mCherry promoter. mTagBFP2 was amplified from pBS mTagBFP2 (derived from pCS2+ mTagBFP2-LL2, gift from Carson Stuckenholz) with F-aactagagattcttgtttaGGAACAAAAGCTGGAGCTCCACC, R-tgaattggctatggtcgacgAATTCCTGCAGCCCGGGG and inserted using HiFi Assembly. To flip the CMV promoter (to generate the CMV:BFP version), the plasmid was cut with BamHI (flanks both sides of CMV) and re-ligated. Candidate regulatory regions were amplified from genomic DNA (~800-1200 bp) and cloned into the plasmid cut with EcoRI/HindIII using HiFi assembly or classical cloning. Primers are listed in Supp. Table 3. Sequences were verified by whole plasmid sequencing (Plasmidsaurus) and concentrations quantified by Qubit.

30 pg of each reporter plasmid was injected into dechorionated 1-cell embryos into the cell using a PV 820 Pneumatic Pico Pump. Fluorescence was visualized at 6 h.p.f. on a Leica M165 FC scope with a FlexCam C3 camera with the following settings: Gamma: 1.5, Sharpness: 10, Noise Reduction: 4, Saturation: 0. For each fluorophore, settings were: mCherry, Exposure 125 ms, Gain 35 dB; BFP: Exposure 125 ms, Gain 28 dB; GFP: Exposure 88.3 ms, Gain 22 dB. Images were edited in Adobe Photoshop using the Levels function, setting the output levels to be (Shadows/Gamma/Highlights): mCherry 30/1/55, GFP 14/1.13/122, BFP 38/0.62/124.

CRISPR mutagenesis

Cas9 crRNAs were designed referring to the IDT design tool and CRISPRscan (Moreno-Mateos et al., 2015) and synthesized by IDT (Alt-R-XT for *albino* and *ier5l*, Alt-R for *hapstr1b*) and resuspended to 100 µM in IDT duplex buffer. crRNAs were hybridized with tracrRNA (IDT) and complexed with Cas9 protein (Alt-R S.p Cas9 Nuclease 3NLS, IDT #1074181) as described in (Hoshijima et al., 2019): final concentration 10 µM Cas9, 10 µM gRNA duplex (equimolar pool of multiple guides), 0.04% Phenol red in a 5 µL volume. CRISPR crRNA sequences: *hapstr1b (*ENSDARG00000012458) enhancer: GGTGACATTGTACTGAGTGG, TGTTAGCTGCTGACCCCTAG, TCTTTGATGAGAAATGAGCG. *ier5l* (ENSDARG00000054906) proximal enhancer: TCCGGTGGCAGGAGGACCAG, ACAACAGTAGGCTACCATGG. *ier5l* distal enhancer: TGCGCGCTGCAGGGTGACAG, CGTGGAAGTGTTAGCAGCAC. *slc45a2* (ENSDARG00000002593, *albino*) promoter (negative control): TCAAGACTTGTGAGCTGAGA, TCCTGCTGGGAGTGGACAAT. Guides were pooled per gene for each set of injections (i.e., all three *hapstr1b* guide were pooled, all four *ier5l* guides were pooled).

Dechorionated 1-cell embryos were injected with 1 nL Cas9 complex into the cell. Embryos were incubated at 28.5ºC and a portion were collected at sphere stage, individually flash frozen in liquid nitrogen, and RNA was extracted by TRIzol (Invitrogen #15596026), quantified by NanoDrop, and stored at -80ºC until use for qRT-PCR. Sibling embryos were collected at 32 hours post-fertilization for genotyping: individual embryos were boiled at 95ºC in 100 mM NaOh for 20 minutes, followed by neutralization with 1 M Tris-HCl (pH 7.4) and stored at -20ºC until use.

For qRT-PCR, 40 ng RNA per embryo was used as template for the Luna Universal One-Step RT-qPCR Kit (NEB #E3005S) with three technical replicates per embryo per primer pair. qRT-PCR was carried out on a QuantStudio 3 96-Well 0.1mL Block machine with the following cycling conditions: an initial 10 minute incubation at 55ºC, followed by 40 cycles of 95ºC, 10s; 60º C, one minute. Ramp speed was 1.6ºC/s. Ct values for technical replicates were averaged, then per embryo Ct values for the target gene (*hapstr1b* or *ier5l*) were normalized to the reference gene (*dusp6* ENSDARG00000070914, an NPS-dependent zygotic gene to control for ZGA timing) (ΔCt). Values were converted to 2^-ΔCt and then normalized by the control embryo average so that the control embryo average value was 1 (0 on a log scale) for graphing. Primers were: *dusp6*: F-AGCCATCAGCTTTATTGATGAG and R-CAAAGTCCAAGAGTTGACCC (209 bp exon 2-3), *hapstr1b*: F-TGTGTGTGTTATTTGAACGGGA and R-TAGGTTAGTGACGGCAGTTG (158 bp exon 2 +

intron, nascent transcript), *ier5l*: F-TGCAGTGGATGCACAAAGTC and R-ATCTCCGCGTACTTCTCGTT (156 bp, single-exon gene).

For genotyping, 1 µL of template was used in a 25 µL PCR reaction (NEB 2x Ultra Q5 master mix, #M0544S), Ta = 67ºC, 30 sec ext., and run on a 2% TAE gel. Genotyping for *ier5l* enhancer deletion involved amplifying each enhancer locus separately, then in another reaction amplifying the region spanning both enhancers using the distal forward and proximal reverse primers to detect large deletions. Primers were: *hapstr1b* enhancer: F-TTCAGCACACATTTCTTTTCTGT, R-AGACAGCCTTCAACAATACACA, *ier5l* distal enhancer: F-CCATTGGATTCGTGACGCAC, R-TACTTGCGTGCCTACTCCTC, *ier5l* proximal enhancer: F-TCGTGGGTTATTCTTTTACGCC, R-TTGAAGTGTGTTTTGCGTTGC.

Data analysis

For CUT&RUN analyses, paired-end reads were mapped to the zebrafish genome (GRCz11) using bowtie2 v2.4.2 (Langmead and Salzberg, 2012) (--no-mixed --no-discordant -X 650). Filtered FASTQ files for each CUT&RUN library were first assembled by removing contaminating read pairs that align the hg38 human genome and not the zebrafish genome (GRCz11). High-quality alignments to zebrafish (MAPQ ≥ 30) were retained, after additional filtering to also exclude reads mapping chrM, or to satellite DNA or rRNA as annotated by RepeatMasker. For the PCA analysis, only mononucleosome-sized CUT&RUN fragments (140 - 250 bp spanned by read pair) were used, which were trimmed (tag-centered) to 73 bp, then filtered to exclude duplicate regions with identical start/end coordinates. To normalize triptolide CUT&RUN samples with yeast spike in, unaligned reads were aligned to the sacCer3 genome to obtain the number of total unique yeast read pairs, and BigWigs were scaled by 1e6/yeast pairs. Downstream analyses were performed using Linux shell scripts with the aid of UCSC Genome Browser - Kent tools (Kent et al., 2010), BEDtools v2.30.0 (Quinlan and Hall, 2010), Samtools v1.12 (Li et al., 2009), and deepTools v3.5.1 (Ramírez et al., 2014).

Accessible regions were defined using ATAC-seq datasets from Liu et al, GEO: GSE101779 (Liu et al., 2018) and Pálfy et al, GEO: GSE130944 (Pálfy et al., 2019) (All public datasets used are listed in Supp. Table 4). For the Liu et al dataset, reads from 1k-cell, oblong, and dome stages were aligned to GRCz11 using bowtie2 (--no-mixed --no-discordant --dovetail -X 2000), retaining read pairs with MAPQ > 2 with fragment length < 120 bp. Reads were clipped using Trim Galore (-e 0.2) (Krueger et al., 2023) prior to mapping. Peaks were called on the union of the stages using Macs2 (Zhang et al., 2008) with an effective genome size of 4.59e8 (GRCz11 summed chromosome length minus sum RepeatMasker annotated regions).

For the Pálfy dataset, published accessible regions were lifted over from GRCz10 to GRCz11, then regions not overlapping the Liu peaks were added to the analysis. In total, there were N = 41,334 accessible regions from the Liu dataset (each region named in the form atac_L00001, atac_L00002, ..., atac_L41334) and N = 7,256 additional regions from the Pálfy dataset (atac_P00001, ..., atac_P07256), for a grand total of N = 48,590 regions.

To identify promoters, published CAGE-Seq data from dome, shield, and 14-somite stages, SRA: SRP013950 (Haberle et al., 2014) was used in conjunction with Ensembl r100 gene annotations to select the maximally zygotically expressed TSS per Ensembl gene (supported by >20 cage tags). Additional TSSs for genes not annotated by Ensembl were added from RefSeq and UMMS v4.3.2 (Lawson et al., 2020) annotations. ATAC-seq accessible regions that overlap a TSS were annotated as a promoter (N = 10,299). To classify enhancers, all remaining ATAC-seq accessible regions <2 kb from any annotated TSS transcript isoform were classified as TSS-proximal elements (alternate promoters or proximal enhancers, N = 11,899), while regions ≥2 kb from any annotated TSS were classified as distal elements, i.e. enhancers (N = 26,197). ATAC-seq open regions on unassembled scaffolds lacking annotated genes were discarded, leaving N = 48,395 total regions.

Raw CUT&RUN read coverage was calculated over the promoter and distal regions using bedtools coverage in the ATAC-seq open interval, 500 bp upstream the interval, and 500 bp downstream the interval (3 counts per ATAC region, per CUT&RUN sample). 63 intervals lacking 500 bp of flanking sequence (e.g., on the edge of a scaffold) were discarded. For PCA, dome stage CUT&RUN coverage counts were used, pooling replicates per histone mark and normalizing counts by region length as log2 RPKM/2 (i.e., per 500 bp rather than per 1 kb), adding a pseudocount of 1. PCA was performed using R 4.1.0 prcomp with input matrix of 48,332 regions x 30 features (upstream, center, downstream per histone mark; "downstream" was set to be the flanking region with higher total CUT&RUN coverage summed over all marks).

To define the "promoter-like" enhancers and "enhancer-like" promoters, rotated data for the first 3 PCs were input into an SVM classifier using the R svm function in the e1071 package v1.7-13 using gamma = 1, cost = 1; only Ensembl promoters and distal enhancers were used. The SVM model was used to classify all regions using the predict function. For contour lines on the biplot visualizations (Fig 1E), a 2D density kernel estimation was calculated for the first 2 PCs using the R kde2d function in the MASS package v7.3-54, h = 3, n = 125. For initial heatmap visualization (Fig 1, 2), regions with ≥2-fold H3K4me1 enrichment over IgG and ≥ 10 RPKM coverage in the center+downstream interval were used, N = 4128 typical enhancers, N = 644 promoter-like enhancers, N = 4707 typical promoters, N = 1224 enhancer-like promoters.

For subsequent analysis, refined active enhancer categories were used: ≥2-fold H3K4me1 and ≥1.5-fold H3K27ac enrichment over IgG; and ≥2-fold H3K4me2 for H3K4me2 enhancers or <1.25-fold H3K4me2 enrichment for H3K4me1 enhancers. Poised enhancers with ≤1.5-fold H3K27ac enrichment were also annotated for reference. A subset of TSS-proximal elements were also annotated as potential enhancers if they had <1.25-fold H3K4me3 enrichment, and ≥2-fold H3K4me2 enrichment for potential H3K4me2 enhancers.

CUT&RUN coverage heatmaps were generated using deepTools computeMatrix reference-point (--referencePoint center -b 2500 -a 2500 --binSize 25 --missingDataAsZero) (Ramírez et al., 2014) with adaptive color scales per histone mark: zMin in the plotHeatmap command is set to the mean upstream signal in the leftmost 20 25-bp bins as calculated by computeMatrix, zMax is set to the 90th percentile of the signal in the center 8 bins. CUT&RUN enrichment heatmaps over IgG were plotted using fold-difference bigWigs generated by bigwigCompare (--operation ratio --skipZeroOverZero --pseudocount 0.1 --binSize 50); plotHeatmap colors ranged from zMin 1 (i.e., no enrichment) to zMax 10 for H3K4me1/2, zMax 4 for other marks. All heatmaps are uniformly sorted relative to descending H3K4me1 signal unless otherwise indicated.

To assess RNA-seq signal at putative enhancers, strand-specific RNA-seq coverage was calculated in a 100 bp window upstream and downstream (relative to genomic coordinates) of each ATAC-seq open interval, using poly(A)+ RNA-seq data at dome, 50% epiboly, shield, and 75% epiboly stages from (White et al., 2017). Potential (+)-strand gene TSSs were regions with ≥1 RPKM (+)-strand coverage downstream that is ≥2-fold higher than (+)-strand coverage upstream, in at least two samples; (-) strand, ≥1 RPKM (-)-strand coverage upstream ≥2-fold higher than downstream. ATAC-seq open regions whose 100 bp flanks fall within a known annotated exon were not considered potential TSSs (i.e., RNA-seq signal is likely due to the surrounding gene).

For other chromatin dataset comparisons: NPS motif density was calculated in a +/- 100 bp window centered on the ATAC-seq open interval using the homer2 find command (Heinz et al., 2010) on empirically determined Nanog, Pou5f3, and Sox19b motifs from performing homer2 de novo motif finding on zebrafish ChIP-seq (Miao et al., 2022). A bigWig of motif hit coordinates/occurrences was used as input to deepTools. Wild-type versus MZ*nps* chromatin heatmaps were generated using deepTools bigwigCompare (--operation log2 --skipZeroOverZero --pseudocount 0.01). DNA methylation was visualized by processing previously published bisulfite sequencing, SRA:SRP020008 (Potok et al., 2013) using bwa-meth (Pedersen et al., 2014) and MethylDackel extract (--mergeContext --minDepth 10)

(github.com/dpryan79/methyldackel). Heatmaps for methylation proportion were generated using computeMatrix --binSize 100 and omitting the --missingDataAsZero parameter, and plotHeatmap using --interpolationMethod nearest to improve aesthetics. For chromatin feature boxplots, average signal over the central 500 bp for histone features or 200 bp for DNA methylation and ATAC-seq was obtained from computeMatrix.

Motif enrichment analysis in enhancer groups was performed using homer2 findMotifs.pl on 200 bp of sequence centered on ATAC open intervals. H3K4me2 enhancer sequences were used as foreground and H3K4me1 enhancer sequences were used as background, then for a separate analysis each enhancer group was used as foreground with background sequences consisting of non-exonic ATAC-seq open regions with < 1.25-fold dome-stage CUT&RUN enrichment for any histone mark (N = 2132). CpG and C+G content was calculated in the center 500 bp of each element using bedtools nuc.

Definitions of NPS-down versus NPS-unaffected genes were obtained from (Miao et al., 2022) (N = 691 down, N = 1100 unaffected). Enhancer distances to each gene group were calculated using bedtools closest, discarding enhancers on unassembled scaffolds. RNA-seq time-course trajectories were calculated for each gene group as the mean log2 expression at each time point minus log2 expression at time 0, using a pseudocount of 0.1. 95% confidence bounds per time point were calculated as +/- qt * standard deviation / sqrt(n) where n = the number of genes and qt is the 0.975 quantile of the t distribution with n-1 degrees of freedom. Published normalized expression values from each study were used and joined with the Miao et al gene IDs, with some genes dropping out due to different annotations used between studies. For the Vejnar et al dataset (Vejnar et al., 2019), yeast spike-in normalized unique counts from rRNA-depleted RNA-seq were used. Maternal-zygotic genes were defined as having pooled 2-cell expression at >0.5 RPKM.

Data availability

Sequencing data are available in the Gene Expression Omnibus (GEO) under accession number GSE269795. Analysis scripts are available at github.com/MTLeeLab/zf-k4 .

Author contributions

M.D.H. and M.T.L. conceived of the project, performed the analyses, and wrote the manuscript. J.M.M. contributed some experiments.

Acknowledgements

We thank S. Hainer for providing the pAG-MNase enzyme and C. Stuckenholz for the tagBFP2 plasmid; S. Hainer, K. Arndt, A. Carlson, M. Rebeiz, M. Tsang, C. Kaplan and their labs for equipment use and feedback. This project used the University of Pittsburgh Health Sciences Core at UPMC Children's Hospital Pittsburgh for sequencing and was supported in part by the University of Pittsburgh Center for Research Computing, RRID:SCR_022735, through the resources provided. Specifically, this work used the H2P cluster, which is supported by NSF award number OAC-2117681. M.T.L was supported by NIH grant R35GM137973 and March of Dimes grant 5-FY16-307.

Declaration of Interests

The authors declare no competing interests.

References

Abrams, E.W., Mullins, M.C., 2009. Early zebrafish development: It's in the maternal genes. Curr. Opin. Genet. Dev., Pattern formation and developmental mechanisms 19, 396–403. https://doi.org/10.1016/j.gde.2009.06.002

Akdogan-Ozdilek, B., Duval, K.L., Meng, F.W., Murphy, P.J., Goll, M.G., 2022. Identification of chromatin states during zebrafish gastrulation using CUT&RUN and CUT&Tag. Dev. Dyn. 251, 729–742. https://doi.org/10.1002/dvdy.430

Allen, M.D., Grummitt, C.G., Hilcenko, C., Min, S.Y., Tonkin, L.M., Johnson, C.M., Freund, S.M., Bycroft, M., Warren, A.J., 2006. Solution structure of the nonmethyl-CpG-binding CXXC domain of the leukaemia-associated MLL histone methyltransferase. EMBO J. 25, 4503–4512. https://doi.org/10.1038/sj.emboj.7601340

Ayton, P.M., Chen, E.H., Cleary, M.L., 2004. Binding to Nonmethylated CpG DNA Is Essential for Target Recognition, Transactivation, and Myeloid Transformation by an MLL Oncoprotein. Mol. Cell. Biol. 24, 10470–10478. https://doi.org/10.1128/MCB.24.23.10470-10478.2004

Barral, A., Zaret, K.S., 2024. Pioneer factors: roles and their regulation in development. Trends Genet. 40, 134–148. https://doi.org/10.1016/j.tig.2023.10.007

Barski, A., Cuddapah, S., Cui, K., Roh, T.-Y., Schones, D.E., Wang, Z., Wei, G., Chepelev, I., Zhao, K., 2007. High-Resolution Profiling of Histone Methylations in the Human Genome. Cell 129, 823–837. https://doi.org/10.1016/j.cell.2007.05.009

Birke, M., Schreiner, S., García-Cuéllar, M.-P., Mahr, K., Titgemeyer, F., Slany, R.K., 2002. The MT domain of the proto-oncoprotein MLL binds to CpG-containing DNA and discriminates against methylation. Nucleic Acids Res. 30, 958–965. https://doi.org/10.1093/nar/30.4.958

Blatt, P., Wong-Deyrup, S.W., McCarthy, A., Breznak, S., Hurton, M.D., Upadhyay, M., Bennink, B., Camacho, J., Lee, M.T., Rangan, P., 2021. RNA degradation is required for the germ-cell to maternal transition in Drosophila. Curr. Biol. 31, 2984-2994.e7. https://doi.org/10.1016/j.cub.2021.04.052

Blythe, S.A., Wieschaus, E.F., 2016. Establishment and maintenance of heritable chromatin structure during early Drosophila embryogenesis. eLife 5, e20148. https://doi.org/10.7554/eLife.20148

Bogdanovic, O., Fernandez-Minan, A., Tena, J.J., de la Calle-Mustienes, E., Hidalgo, C., van Kruysbergen, I., van Heeringen, S.J., Veenstra, G.J.C., Gomez-Skarmeta, J.L., 2012. Dynamics of enhancer chromatin signatures mark the transition from pluripotency to cell specification during embryogenesis. Genome Res. 22, 2043–2053. https://doi.org/10.1101/gr.134833.111

Chan, S.H., Tang, Y., Miao, L., Darwich-Codore, H., Vejnar, C.E., Beaudoin, J.-D., Musaev, D., Fernandez, J.P., Benitez, M.D.J., Bazzini, A.A., Moreno-Mateos, M.A., Giraldez, A.J., 2019. Brd4 and P300 Confer Transcriptional Competency during Zygotic Genome Activation. Dev. Cell 49, 867-881.e8. https://doi.org/10.1016/j.devcel.2019.05.037

Colonnetta, M.M., Abrahante, J.E., Schedl, P., Gohl, D.M., Deshpande, G., 2021. CLAMP regulates zygotic genome activation in Drosophila embryos. Genetics 219, iyab107. https://doi.org/10.1093/genetics/iyab107

Duan, J., Rieder, L., Colonnetta, M.M., Huang, A., Mckenney, M., Watters, S., Deshpande, G., Jordan, W., Fawzi, N., Larschan, E., 2021. CLAMP and Zelda function together to promote Drosophila zygotic genome activation. eLife 10, e69937. https://doi.org/10.7554/eLife.69937

Dubrulle, J., Jordan, B.M., Akhmetova, L., Farrell, J.A., Kim, S.-H., Solnica-Krezel, L., Schier, A.F., 2015. Response to Nodal morphogen gradient is determined by the kinetics of target gene induction. eLife 4, e05042. https://doi.org/10.7554/eLife.05042

781 Duval, K.L., Artis, A.R., Goll, M.G., 2024. The emerging H3K9me3 chromatin landscape during
782 zebrafish embryogenesis. https://doi.org/10.1101/2024.03.05.582530
783 Ernst, J., Kheradpour, P., Mikkelsen, T.S., Shoresh, N., Ward, L.D., Epstein, C.B., Zhang, X.,
784 Wang, L., Issner, R., Coyne, M., others, 2011. Mapping and analysis of chromatin state
785 dynamics in nine human cell types. Nature 473, 43–49.
786 Esmaeili, M., Blythe, S.A., Tobias, J.W., Zhang, K., Yang, J., Klein, P.S., 2020. Chromatin
787 accessibility and histone acetylation in the regulation of competence in early
788 development. Dev. Biol. 462, 20–35. https://doi.org/10.1016/j.ydbio.2020.02.013
789 Gao, M., Veil, M., Rosenblatt, M., Riesle, A.J., Gebhard, A., Hass, H., Buryanova, L.,
790 Yampolsky, L.Y., Grüning, B., Ulianov, S.V., Timmer, J., Onichtchouk, D., 2022.
791 Pluripotency factors determine gene expression repertoire at zygotic genome activation.
792 Nat. Commun. 13, 788. https://doi.org/10.1038/s41467-022-28434-1
793 Gaskill, M.M., Gibson, T.J., Larson, E.D., Harrison, M.M., 2021. GAF is essential for zygotic
794 genome activation and chromatin accessibility in the early Drosophila embryo. eLife 10,
795 e66668. https://doi.org/10.7554/eLife.66668
796 Gentsch, G.E., Spruce, T., Owens, N.D.L., Smith, J.C., 2019. Maternal pluripotency factors
797 initiate extensive chromatin remodelling to predefine first response to inductive signals.
798 Nat. Commun. 10, 1–22. https://doi.org/10.1038/s41467-019-12263-w
799 Guo, Y., Li, T.D., Modzelewski, A.J., Siomi, H., 2024. Retrotransposon renaissance in early
800 embryos. Trends Genet. 40, 39–51. https://doi.org/10.1016/j.tig.2023.10.010
801 Haberle, V., Li, N., Hadzhiev, Y., Plessy, C., Previti, C., Nepal, C., Gehrig, J., Dong, X., Akalin,
802 A., Suzuki, A.M., van lJcken, W.F.J., Armant, O., Ferg, M., Strähle, U., Carninci, P.,
803 Müller, F., Lenhard, B., 2014. Two independent transcription initiation codes overlap on
804 vertebrate core promoters. Nature 507, 381–385. https://doi.org/10.1038/nature12974
805 Hadzhiev, Y., Wheatley, L., Cooper, L., Ansaloni, F., Whalley, C., Chen, Z., Finaurini, S.,
806 Gustincich, S., Sanges, R., Burgess, S., Beggs, A., Müller, F., 2023. The miR-430 locus
807 with extreme promoter density forms a transcription body during the minor wave of
808 zygotic genome activation. Dev. Cell 58, 155-170.e8.
809 https://doi.org/10.1016/j.devcel.2022.12.007
810 Hainer, S.J., Bošković, A., McCannell, K.N., Rando, O.J., Fazzio, T.G., 2019. Profiling of
811 Pluripotency Factors in Single Cells and Early Embryos. Cell 177, 1319-1329.e11.
812 https://doi.org/10.1016/j.cell.2019.03.014
813 Hansen, J.L., Cohen, B.A., 2022. A quantitative metric of pioneer activity reveals that HNF4A
814 has stronger in vivo pioneer activity than FOXA1. Genome Biol. 23, 221.
815 https://doi.org/10.1186/s13059-022-02792-x
816 Harvey, S.A., Sealy, I., Kettleborough, R., Fenyes, F., White, R., Stemple, D., Smith, J.C., 2013.
817 Identification of the zebrafish maternal and paternal transcriptomes. Dev. Camb. Engl.
818 140, 2703–2710. https://doi.org/10.1242/dev.095091
819 Heintzman, N.D., Stuart, R.K., Hon, G., Fu, Y., Ching, C.W., Hawkins, R.D., Barrera, L.O., Van
820 Calcar, S., Qu, C., Ching, K.A., Wang, W., Weng, Z., Green, R.D., Crawford, G.E., Ren,
821 B., 2007. Distinct and predictive chromatin signatures of transcriptional promoters and
822 enhancers in the human genome. Nat. Genet. 39, 311–318.
823 https://doi.org/10.1038/ng1966
824 Heinz, S., Benner, C., Spann, N., Bertolino, E., Lin, Y.C., Laslo, P., Cheng, J.X., Murre, C.,
825 Singh, H., Glass, C.K., 2010. Simple combinations of lineage-determining transcription
826 factors prime cis-regulatory elements required for macrophage and B cell identities. Mol.
827 Cell 38, 576–589. https://doi.org/10.1016/j.molcel.2010.05.004
828 Herz, H.-M., Mohan, M., Garruss, A.S., Liang, K., Takahashi, Y., Mickey, K., Voets, O.,
829 Verrijzer, C.P., Shilatifard, A., 2012. Enhancer-associated H3K4 monomethylation by
830 Trithorax-related, the Drosophila homolog of mammalian Mll3/Mll4. Genes Dev. 26,
831 2604–2620. https://doi.org/10.1101/gad.201327.112

832 Heyn, P., Kircher, M., Dahl, A., Kelso, J., Tomancak, P., Kalinka, A.T., Neugebauer, K.M., 2014.
833 The earliest transcribed zygotic genes are short, newly evolved, and different across
834 species. Cell Rep. 6, 285–292.
835 Hickey, G.J., Wike, C.L., Nie, X., Guo, Y., Tan, M., Murphy, P.J., Cairns, B.R., 2022.
836 Establishment of developmental gene silencing by ordered polycomb complex
837 recruitment in early zebrafish embryos. eLife 11, e67738.
838 https://doi.org/10.7554/eLife.67738
839 Hoshijima, K., Jurynec, M.J., Shaw, D.K., Jacobi, A.M., Behlke, M.A., Grunwald, D.J., 2019.
840 Highly Efficient CRISPR-Cas9-Based Methods for Generating Deletion Mutations and F0
841 Embryos that Lack Gene Function in Zebrafish. Dev. Cell 51, 645-657.e4.
842 https://doi.org/10.1016/j.devcel.2019.10.004
843 Hu, D., Gao, X., Cao, K., Morgan, M.A., Mas, G., Smith, E.R., Volk, A.G., Bartom, E.T.,
844 Crispino, J.D., Croce, L.D., Shilatifard, A., 2017. Not All H3K4 Methylations Are Created
845 Equal: Mll2/COMPASS Dependency in Primordial Germ Cell Specification. Mol. Cell 65,
846 460-475.e6. https://doi.org/10.1016/j.molcel.2017.01.013
847 Hu, D., Gao, X., Morgan, M.A., Herz, H.-M., Smith, E.R., Shilatifard, A., 2013. The MLL3/MLL4
848 Branches of the COMPASS Family Function as Major Histone H3K4 Monomethylases at
849 Enhancers. Mol. Cell. Biol. 33, 4745–4754. https://doi.org/10.1128/MCB.01181-13
850 Jiang, L., Zhang, Jing, Wang, J.-J., Wang, L., Zhang, L., Li, G., Yang, X., Ma, X., Sun, X., Cai,
851 J., Zhang, Jun, Huang, X., Yu, M., Wang, X., Liu, F., Wu, C.-I., He, C., Zhang, B., Ci, W.,
852 Liu, J., 2013. Sperm, but Not Oocyte, DNA Methylome Is Inherited by Zebrafish Early
853 Embryos. Cell 153, 773–784. https://doi.org/10.1016/j.cell.2013.04.041
854 Joseph, S.R., Pálfy, M., Hilbert, L., Kumar, M., Karschau, J., Zaburdaev, V., Shevchenko, A.,
855 Vastenhouw, N.L., 2017. Competition between histone and transcription factor binding
856 regulates the onset of transcription in zebrafish embryos. eLife 6.
857 https://doi.org/10.7554/eLife.23326
858 Jozwik, K.M., Chernukhin, I., Serandour, A.A., Nagarajan, S., Carroll, J.S., 2016. FOXA1 Directs
859 H3K4 Monomethylation at Enhancers via Recruitment of the Methyltransferase MLL3.
860 Cell Rep. 17, 2715–2723. https://doi.org/10.1016/j.celrep.2016.11.028
861 Kaaij, L.J., Mokry, M., Zhou, M., Musheev, M., Geeven, G., Melquiond, A.S., de Jesus
862 Domingues, A.M., de Laat, W., Niehrs, C., Smith, A.D., others, 2016. Enhancers reside
863 in a unique epigenetic environment during early zebrafish development. Genome Biol.
864 17, 1.
865 Kent, W.J., Zweig, A.S., Barber, G., Hinrichs, A.S., Karolchik, D., 2010. BigWig and BigBed:
866 enabling browsing of large distributed datasets. Bioinformatics 26, 2204–2207.
867 https://doi.org/10.1093/bioinformatics/btq351
868 Koch, F., Andrau, J.-C., 2011. Initiating RNA Polymerase II and TIPs as hallmarks of enhancer
869 activity and tissue-specificity. Transcription 2, 263–268.
870 https://doi.org/10.4161/trns.2.6.18747
871 Kontur, C., Jeong, M., Cifuentes, D., Giraldez, A.J., 2020. Ythdf m6A Readers Function
872 Redundantly during Zebrafish Development. Cell Rep. 33, 108598.
873 https://doi.org/10.1016/j.celrep.2020.108598
874 Krueger, F., James, F., Ewels, P., Afyounian, E., Weinstein, M., Schuster-Boeckler, B.,
875 Hulselmans, G., Sclamons, 2023. FelixKrueger/TrimGalore: v0.6.10 - add default
876 decompression path. https://doi.org/10.5281/ZENODO.5127898
877 Kvon, E.Z., Waymack, R., Gad, M., Wunderlich, Z., 2021. Enhancer redundancy in development
878 and disease. Nat. Rev. Genet. 22, 324–336. https://doi.org/10.1038/s41576-020-00311-x
879 Ladam, F., Stanney, W., Donaldson, I.J., Yildiz, O., Bobola, N., Sagerström, C.G., 2018. TALE
880 factors use two distinct functional modes to control an essential zebrafish gene
881 expression program. eLife 7, e36144. https://doi.org/10.7554/eLife.36144

882 Langmead, B., Salzberg, S.L., 2012. Fast gapped-read alignment with Bowtie 2. Nat. Methods
883 9, 357–359. https://doi.org/10.1038/nmeth.1923
884 Lawson, N.D., Li, R., Shin, M., Grosse, A., Yukselen, O., Stone, O.A., Kucukural, A., Zhu, L.,
885 2020. An improved zebrafish transcriptome annotation for sensitive and comprehensive
886 detection of cell type-specific genes. eLife 9, e55792. https://doi.org/10.7554/eLife.55792
887 Lee, H.J., Lowdon, R.F., Maricque, B., Zhang, B., Stevens, M., Li, D., Johnson, S.L., Wang, T.,
888 2015. Developmental enhancers revealed by extensive DNA methylome maps of
889 zebrafish early embryos. Nat. Commun. 6, 6315. https://doi.org/10.1038/ncomms7315
890 Lee, J.-E., Wang, C., Xu, S., Cho, Y.-W., Wang, L., Feng, X., Baldridge, A., Sartorelli, V.,
891 Zhuang, L., Peng, W., Ge, K., 2013. H3K4 mono- and di-methyltransferase MLL4 is
892 required for enhancer activation during cell differentiation. eLife 2, e01503.
893 https://doi.org/10.7554/eLife.01503
894 Lee, J.-H., Skalnik, D.G., 2005. CpG-binding Protein (CXXC Finger Protein 1) Is a Component
895 of the Mammalian Set1 Histone H3-Lys4 Methyltransferase Complex, the Analogue of
896 the Yeast Set1/COMPASS Complex *. J. Biol. Chem. 280, 41725–41731.
897 https://doi.org/10.1074/jbc.M508312200
898 Lee, M.T., Bonneau, A.R., Giraldez, A.J., 2014. Zygotic genome activation during the maternal-
899 to-zygotic transition. Annu. Rev. Cell Dev. Biol. 30, 581.
900 Lee, M.T., Bonneau, A.R., Takacs, C.M., Bazzini, A.A., DiVito, K.R., Fleming, E.S., Giraldez,
901 A.J., 2013. Nanog, Pou5f1 and SoxB1 activate zygotic gene expression during the
902 maternal-to-zygotic transition. Nature 503, 360–364. https://doi.org/10.1038/nature12632
903 Leichsenring, M., Maes, J., Mössner, R., Driever, W., Onichtchouk, D., 2013. Pou5f1
904 transcription factor controls zygotic gene activation in vertebrates. Science 341, 1005–
905 1009. https://doi.org/10.1126/science.1242527
906 Li, H., Handsaker, B., Wysoker, A., Fennell, T., Ruan, J., Homer, N., Marth, G., Abecasis, G.,
907 Durbin, R., 1000 Genome Project Data Processing Subgroup, 2009. The Sequence
908 Alignment/Map format and SAMtools. Bioinformatics 25, 2078–2079.
909 https://doi.org/10.1093/bioinformatics/btp352
910 Li, Y., Zhao, L., Zhang, Y., Wu, P., Xu, Y., Mencius, J., Zheng, Y., Wang, X., Xu, W., Huang, N.,
911 Ye, X., Lei, M., Shi, P., Tian, C., Peng, C., Li, G., Liu, Z., Quan, S., Chen, Y., 2022.
912 Structural basis for product specificities of MLL family methyltransferases. Mol. Cell 82,
913 3810-3825.e8. https://doi.org/10.1016/j.molcel.2022.08.022
914 Liang, H.-L., Nien, C.-Y., Liu, H.-Y., Metzstein, M.M., Kirov, N., Rushlow, C., 2008. The zinc-
915 finger protein Zelda is a key activator of the early zygotic genome in Drosophila. Nature
916 456, 400–403.
917 Lindeman, L.C., Andersen, I.S., Reiner, A.H., Li, N., Aanes, H., Østrup, O., Winata, C.,
918 Mathavan, S., Müller, F., Aleström, P., Collas, P., 2011. Prepatterning of Developmental
919 Gene Expression by Modified Histones before Zygotic Genome Activation. Dev. Cell 21,
920 993–1004. https://doi.org/10.1016/j.devcel.2011.10.008
921 Liu, B., He, Y., Wu, X., Lin, Z., Ma, J., Qiu, Y., Xiang, Y., Kong, F., Lai, F., Pal, M., Wang, P.,
922 Ming, J., Zhang, B., Wang, Q., Wu, J., Xia, W., Shen, W., Na, J., Torres-Padilla, M.-E.,
923 Li, J., Xie, W., 2024. Mapping putative enhancers in mouse oocytes and early embryos
924 reveals TCF3/12 as key folliculogenesis regulators. Nat. Cell Biol. 26, 962–974.
925 https://doi.org/10.1038/s41556-024-01422-x
926 Liu, G., Wang, W., Hu, S., Wang, X., Zhang, Y., 2018. Inherited DNA methylation primes the
927 establishment of accessible chromatin during genome activation. Genome Res.
928 https://doi.org/10.1101/gr.228833.117
929 Lorenzo-Orts, L., Pauli, A., 2024. The molecular mechanisms underpinning maternal mRNA
930 dormancy. Biochem. Soc. Trans. 52, 861–871. https://doi.org/10.1042/BST20231122
931 Miao, L., Tang, Y., Bonneau, A.R., Chan, S.H., Kojima, M.L., Pownall, M.E., Vejnar, C.E., Gao,
932 F., Krishnaswamy, S., Hendry, C.E., Giraldez, A.J., 2022. The landscape of pioneer

933 factor activity reveals the mechanisms of chromatin reprogramming and genome
934 activation. Mol. Cell 82, 986-1002.e9. https://doi.org/10.1016/j.molcel.2022.01.024
935 Moreno-Mateos, M.A., Vejnar, C.E., Beaudoin, J.-D., Fernandez, J.P., Mis, E.K., Khokha, M.K.,
936 Giraldez, A.J., 2015. CRISPRscan: designing highly efficient sgRNAs for CRISPR-Cas9
937 targeting in vivo. Nat. Methods 12, 982–988.
938 Murphy, P.J., Wu, S.F., James, C.R., Wike, C.L., Cairns, B.R., 2018. Placeholder Nucleosomes
939 Underlie Germline-to-Embryo DNA Methylation Reprogramming. Cell 172, 993-
940 1006.e13. https://doi.org/10.1016/j.cell.2018.01.022
941 Narita, T., Higashijima, Y., Kilic, S., Liebner, T., Walter, J., Choudhary, C., 2023. Acetylation of
942 histone H2B marks active enhancers and predicts CBP/p300 target genes. Nat. Genet.
943 55, 679–692. https://doi.org/10.1038/s41588-023-01348-4
944 Pálfy, M., Schulze, G., Valen, E., Vastenhouw, N.L., 2019. Chromatin accessibility established
945 by Pou5f3, Sox19b and Nanog primes genes for activity during zebrafish genome
946 activation. bioRxiv 639302. https://doi.org/10.1101/639302
947 Paraiso, K.D., Blitz, I.L., Coley, M., Cheung, J., Sudou, N., Taira, M., Cho, K.W.Y., 2019.
948 Endodermal Maternal Transcription Factors Establish Super-Enhancers during Zygotic
949 Genome Activation. Cell Rep. 27, 2962-2977.e5.
950 https://doi.org/10.1016/j.celrep.2019.05.013
951 Pedersen, B.S., Eyring, K., De, S., Yang, I.V., Schwartz, D.A., 2014. Fast and accurate
952 alignment of long bisulfite-seq reads. https://doi.org/10.48550/arXiv.1401.1129
953 Pekowska, A., Benoukraf, T., Zacarias-Cabeza, J., Belhocine, M., Koch, F., Holota, H., Imbert,
954 J., Andrau, J.-C., Ferrier, P., Spicuglia, S., 2011. H3K4 tri-methylation provides an
955 epigenetic signature of active enhancers. EMBO J. 30, 4198–4210.
956 https://doi.org/10.1038/emboj.2011.295
957 Phelps, W.A., Hurton, M.D., Ayers, T.N., Carlson, A.E., Rosenbaum, J.C., Lee, M.T., 2023.
958 Hybridization led to a rewired pluripotency network in the allotetraploid Xenopus laevis.
959 eLife 12, e83952. https://doi.org/10.7554/eLife.83952
960 Potok, M.E., Nix, D.A., Parnell, T.J., Cairns, B.R., 2013. Reprogramming the maternal zebrafish
961 genome after fertilization to match the paternal methylation pattern. Cell 153, 759–772.
962 Pradeepa, M.M., Grimes, G.R., Kumar, Y., Olley, G., Taylor, G.C.A., Schneider, R., Bickmore,
963 W.A., 2016. Histone H3 globular domain acetylation identifies a new class of enhancers.
964 Nat. Genet. 48, 681–686. https://doi.org/10.1038/ng.3550
965 Quinlan, A.R., Hall, I.M., 2010. BEDTools: a flexible suite of utilities for comparing genomic
966 features. Bioinformatics 26, 841–842. https://doi.org/10.1093/bioinformatics/btq033
967 Ramírez, F., Dündar, F., Diehl, S., Grüning, B.A., Manke, T., 2014. deepTools: a flexible
968 platform for exploring deep-sequencing data. Nucleic Acids Res. 42, W187–W191.
969 https://doi.org/10.1093/nar/gku365
970 Riesle, A.J., Gao, M., Rosenblatt, M., Hermes, J., Hass, H., Gebhard, A., Veil, M., Grüning, B.,
971 Timmer, J., Onichtchouk, D., 2023. Activator-blocker model of transcriptional regulation
972 by pioneer-like factors. Nat. Commun. 14, 5677. https://doi.org/10.1038/s41467-023-
973 41507-z
974 Shah, R.N., Grzybowski, A.T., Cornett, E.M., Johnstone, A.L., Dickson, B.M., Boone, B.A.,
975 Cheek, M.A., Cowles, M.W., Maryanski, D., Meiners, M.J., Tiedemann, R.L., Vaughan,
976 R.M., Arora, N., Sun, Z.-W., Rothbart, S.B., Keogh, M.-C., Ruthenburg, A.J., 2018.
977 Examining the Roles of H3K4 Methylation States with Systematically Characterized
978 Antibodies. Mol. Cell 72, 162-177.e7. https://doi.org/10.1016/j.molcel.2018.08.015
979 Skene, P.J., Henikoff, S., 2017. An efficient targeted nuclease strategy for high-resolution
980 mapping of DNA binding sites. Elife 6, e21856.
981 Soufi, A., Garcia, M.F., Jaroszewicz, A., Osman, N., Pellegrini, M., Zaret, K.S., 2015. Pioneer
982 Transcription Factors Target Partial DNA Motifs on Nucleosomes to Initiate
983 Reprogramming. Cell 161, 555–568. https://doi.org/10.1016/j.cell.2015.03.017

Stanney, W., Ladam, F., Donaldson, I.J., Parsons, T.J., Maehr, R., Bobola, N., Sagerström, C.G., 2020. Combinatorial action of NF–Y and TALE at embryonic enhancers defines distinct gene expression programs during zygotic genome activation in zebrafish. Dev. Biol. 459, 161–180. https://doi.org/10.1016/j.ydbio.2019.12.003

Svoboda, P., 2018. Mammalian zygotic genome activation. Semin. Cell Dev. Biol., SI: Antigen presentation 84, 118–126. https://doi.org/10.1016/j.semcdb.2017.12.006

Tan, Y., Xue, Y., Song, C., Grunstein, M., 2013. Acetylated histone H3K56 interacts with Oct4 to promote mouse embryonic stem cell pluripotency. Proc. Natl. Acad. Sci. 110, 11493–11498. https://doi.org/10.1073/pnas.1309914110

ten Bosch, J.R., Benavides, J.A., Cline, T.W., 2006. The TAGteam DNA motif controls the timing of Drosophila pre-blastoderm transcription. Dev. Camb. Engl. 133, 1967.

Van, H.T., Xie, G., Dong, P., Liu, Z., Ge, K., 2024. KMT2 Family of H3K4 Methyltransferases: Enzymatic Activity-dependent and -independent Functions. J. Mol. Biol., Interpreting Combinatorial Epigenetic Modifications for Biological Meaning 436, 168453. https://doi.org/10.1016/j.jmb.2024.168453

Vastenhouw, N.L., Cao, W.X., Lipshitz, H.D., 2019. The maternal-to-zygotic transition revisited. Development 146, dev161471. https://doi.org/10.1242/dev.161471

Vastenhouw, N.L., Zhang, Y., Woods, I.G., Imam, F., Regev, A., Liu, X.S., Rinn, J., Schier, A.F., 2010. Chromatin signature of embryonic pluripotency is established during genome activation. Nature 464, 922–926. https://doi.org/10.1038/nature08866

Veil, M., Yampolsky, L.Y., Grüning, B., Onichtchouk, D., 2019. Pou5f3, SoxB1, and Nanog remodel chromatin on high nucleosome affinity regions at zygotic genome activation. Genome Res. 29, 383–395. https://doi.org/10.1101/gr.240572.118

Vejnar, C.E., Abdel Messih, M., Takacs, C.M., Yartseva, V., Oikonomou, P., Christiano, R., Stoeckius, M., Lau, S., Lee, M.T., Beaudoin, J.-D., Musaev, D., Darwich-Codore, H., Walther, T.C., Tavazoie, S., Cifuentes, D., Giraldez, A.J., 2019. Genome wide analysis of 3' UTR sequence elements and proteins regulating mRNA stability during maternal-to-zygotic transition in zebrafish. Genome Res. 29, 1100–1114. https://doi.org/10.1101/gr.245159.118

Wang, C., Lee, J.-E., Lai, B., Macfarlan, T.S., Xu, S., Zhuang, L., Liu, C., Peng, W., Ge, K., 2016. Enhancer priming by H3K4 methyltransferase MLL4 controls cell fate transition. Proc. Natl. Acad. Sci. 113, 11871–11876. https://doi.org/10.1073/pnas.1606857113

Wang, H., Helin, K., 2024. Roles of H3K4 methylation in biology and disease. Trends Cell Biol. 0. https://doi.org/10.1016/j.tcb.2024.06.001

White, R.J., Collins, J.E., Sealy, I.M., Wali, N., Dooley, C.M., Digby, Z., Stemple, D.L., Murphy, D.N., Billis, K., Hourlier, T., Füllgrabe, A., Davis, M.P., Enright, A.J., Busch-Nentwich, E.M., 2017. A high-resolution mRNA expression time course of embryonic development in zebrafish. eLife 6, e30860. https://doi.org/10.7554/eLife.30860

Wu, Xiaotong, Zhang, H., Zhang, B., Zhang, Y., Wang, Q., Shen, W., Wu, Xi, Li, L., Xia, W., Nakamura, R., Liu, B., Liu, F., Takeda, H., Meng, A., Xie, W., 2021. Methylome inheritance and enhancer dememorization reset an epigenetic gate safeguarding embryonic programs. Sci. Adv. 7, eabl3858. https://doi.org/10.1126/sciadv.abl3858

Xu, C., Fan, Z.P., Müller, P., Fogley, R., DiBiase, A., Trompouki, E., Unternaehrer, J., Xiong, F., Torregroza, I., Evans, T., Megason, S.G., Daley, G.Q., Schier, A.F., Young, R.A., Zon, L.I., 2012. Nanog-like Regulates Endoderm Formation through the Mxtx2-Nodal Pathway. Dev. Cell 22, 625–638. https://doi.org/10.1016/j.devcel.2012.01.003

Yan, C., Chen, H., Bai, L., 2018. Systematic Study of Nucleosome-Displacing Factors in Budding Yeast. Mol. Cell 71, 294-305.e4. https://doi.org/10.1016/j.molcel.2018.06.017

Zentner, G.E., Tesar, P.J., Scacheri, P.C., 2011. Epigenetic signatures distinguish multiple classes of enhancers with distinct cellular functions. Genome Res. 21, 1273–1283. https://doi.org/10.1101/gr.122382.111

1035 Zhang, B., Wu, X., Zhang, W., Shen, W., Sun, Q., Liu, K., Zhang, Y., Wang, Q., Li, Y., Meng, A.,
1036 Xie, W., 2018. Widespread Enhancer Dememorization and Promoter Priming during
1037 Parental-to-Zygotic Transition. Mol. Cell 72, 673-686.e6.
1038 https://doi.org/10.1016/j.molcel.2018.10.017
1039 Zhang, H., Gayen, S., Xiong, J., Zhou, B., Shanmugam, A.K., Sun, Y., Karatas, H., Liu, L., Rao,
1040 R.C., Wang, S., Nesvizhskii, A.I., Kalantry, S., Dou, Y., 2016. MLL1 Inhibition
1041 Reprograms Epiblast Stem Cells to Naive Pluripotency. Cell Stem Cell 18, 481–494.
1042 https://doi.org/10.1016/j.stem.2016.02.004
1043 Zhang, Y., Liu, T., Meyer, C.A., Eeckhoute, J., Johnson, D.S., Bernstein, B.E., Nussbaum, C.,
1044 Myers, R.M., Brown, M., Li, W., Liu, X.S., 2008. Model-based Analysis of ChIP-Seq
1045 (MACS). Genome Biol. 9, R137. https://doi.org/10.1186/gb-2008-9-9-r137
1046 Zhang, Y., Vastenhouw, N.L., Feng, J., Fu, K., Wang, C., Ge, Y., Pauli, A., van Hummelen, P.,
1047 Schier, A.F., Liu, X.S., 2014. Canonical nucleosome organization at promoters forms
1048 during genome activation. Genome Res. 24, 260–266.
1049 Zhao, Y., Garcia, B.A., 2015. Comprehensive Catalog of Currently Documented Histone
1050 Modifications. Cold Spring Harb. Perspect. Biol. 7, a025064.
1051 https://doi.org/10.1101/cshperspect.a025064
1052 Zhu, W., Xu, X., Wang, X., Liu, J., 2019. Reprogramming histone modification patterns to
1053 coordinate gene expression in early zebrafish embryos. BMC Genomics 20, 248.
1054 https://doi.org/10.1186/s12864-019-5611-7

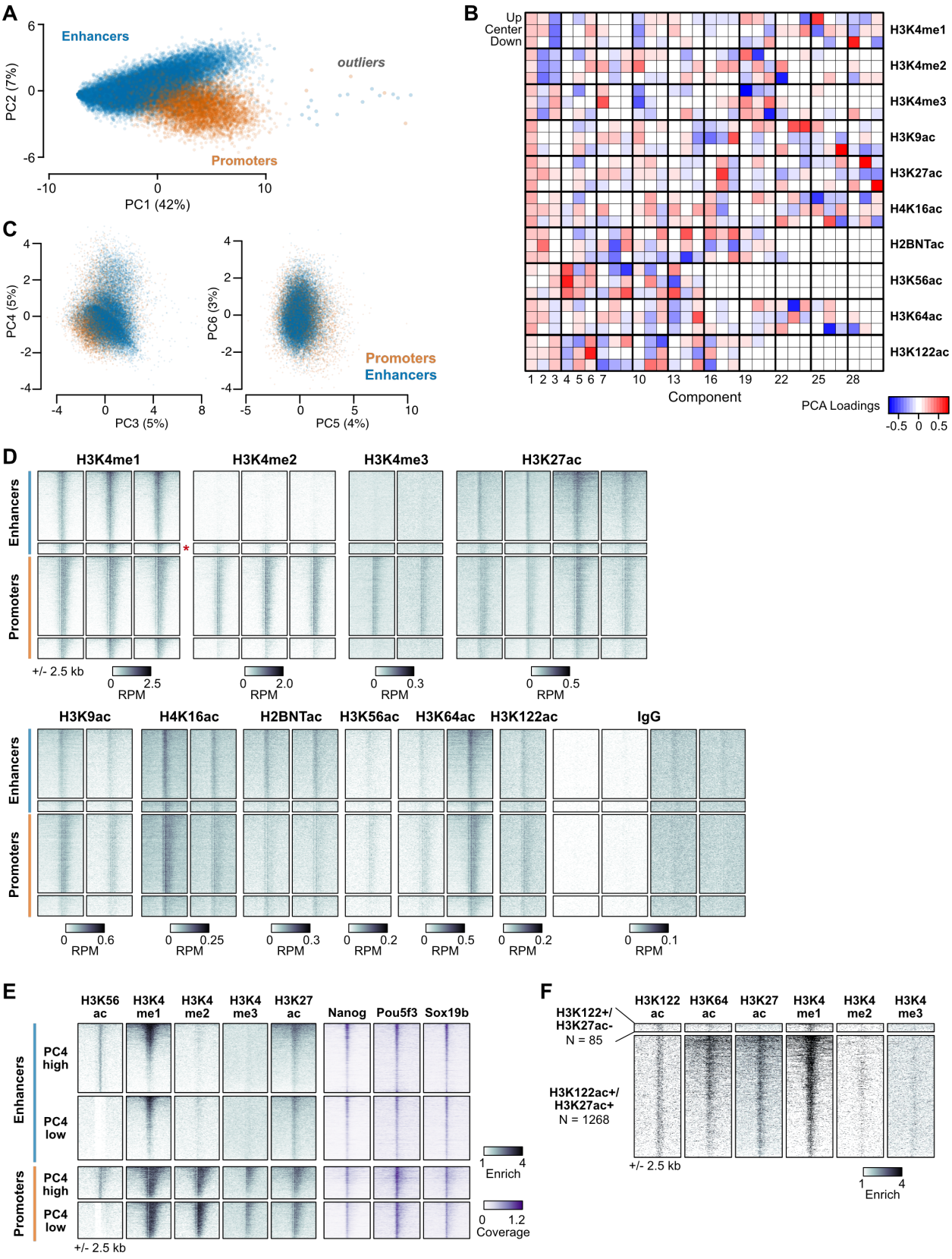

Supplementary Figure 1. Principal component analysis on histone modifications. (A) Full biplot of the first two principal components (PCs) as in Fig. 1D, including outliers far from the main point masses. Percent of total variance explained per PC in parentheses. Points are labeled as enhancers (blue) or promoters (orange). **(B)** Heatmap of the loadings from the PCA. Columns are principal components, rows are input variables – histone modification coverage on upstream, center, and downstream regions of predicted regulatory elements. **(C)** Biplots as in (A) for PCs 3 through 6. **(D)** Heatmaps of CUT&RUN coverage as in Fig 1F showing individual replicates. **(E)** Heatmaps of regions stratified by the fourth PC, which loads heavily on H3K56ac. PC4 high = greater than the standard deviation of PC4, PC4 low = less than -1 * standard deviation of PC4. Parallel heatmaps of Nanog, Pou5f3, and Sox19b ChIP-seq coverage (data from Miao et al, 2022) demonstrate minimal differences correlated with PC4, in contrast to mouse ES cells in which Pou5f3 homolog Oct4 correlates with H3K56ac (Tan et al, 2013). **(F)** Heatmaps of regions enriched for H3K122ac (>2-fold over IgG), stratified by H3K27ac co-enrichment (<1.25-fold or >1.5-fold).

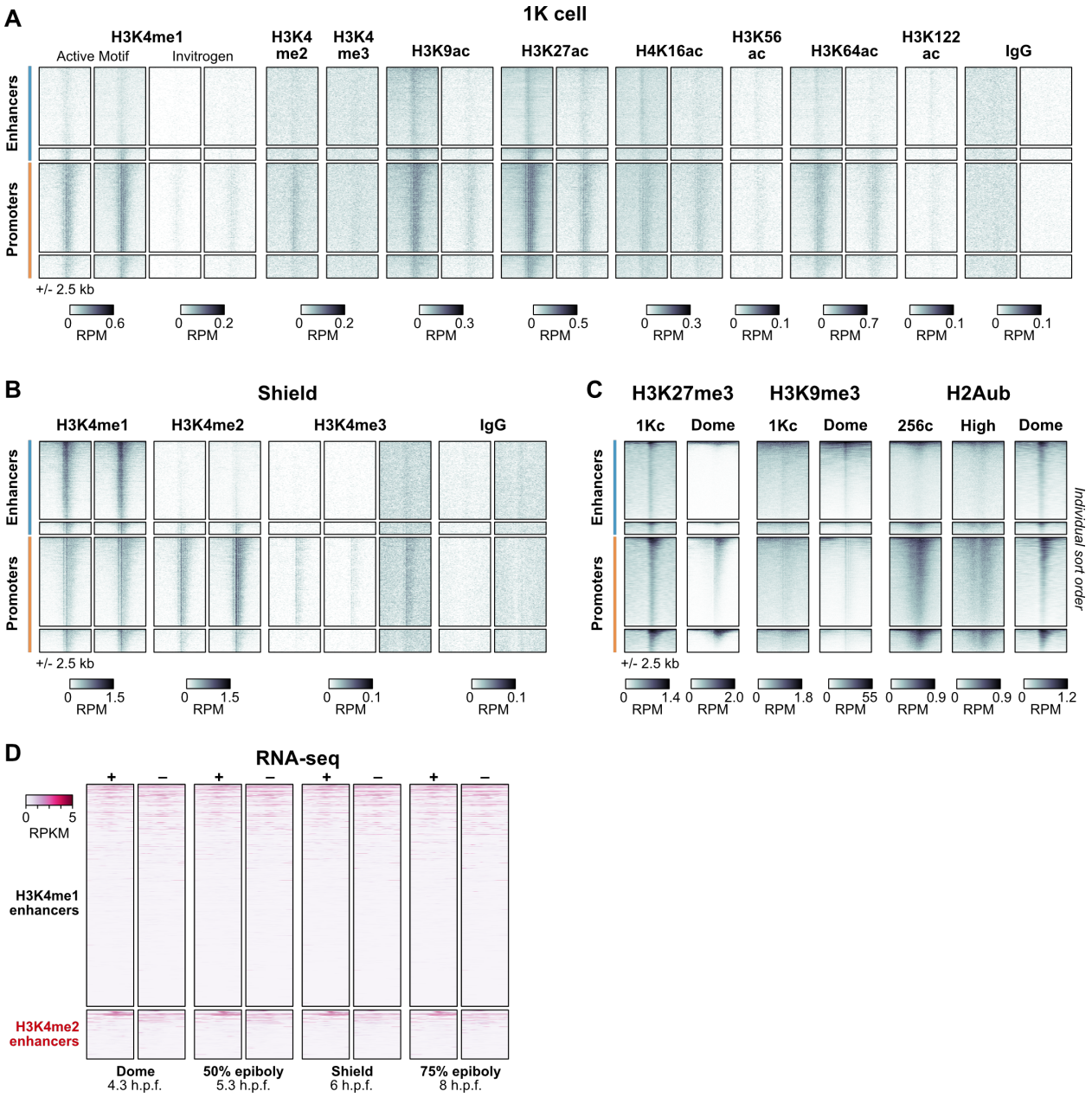

Supplementary Figure 2. Genomic profiles over time. (A) Heatmaps of CUT&RUN coverage for histone modifications at 1K-cell stage centered on enhancer and promoter regions as defined in Fig. 1F. Individual replicates are shown. Two different H3K4me1 antibodies were used, Active Motif #39297 and Invitrogen #710795 (the same antibody used for all other time points). **(B)** Heatmaps of CUT&RUN coverage at shield stage showing individual replicates. **(C)** Heatmaps of ChIP-seq for repressive histone modifications. Each heatmap is sorted by descending signal per region group independently. Data are from Zhu et al, 2019 (1K-cell H3K27me3), Zhang et al, 2014 (dome H3K27me3), Duval et al, 2024 (H3K9me3), and Hickey et al, 2022 (H2Aub). **(D)** Strand-separated RNA-seq coverage heatmaps as in Fig. 2B showing intermediate developmental stages. Data are from White et al, 2017.

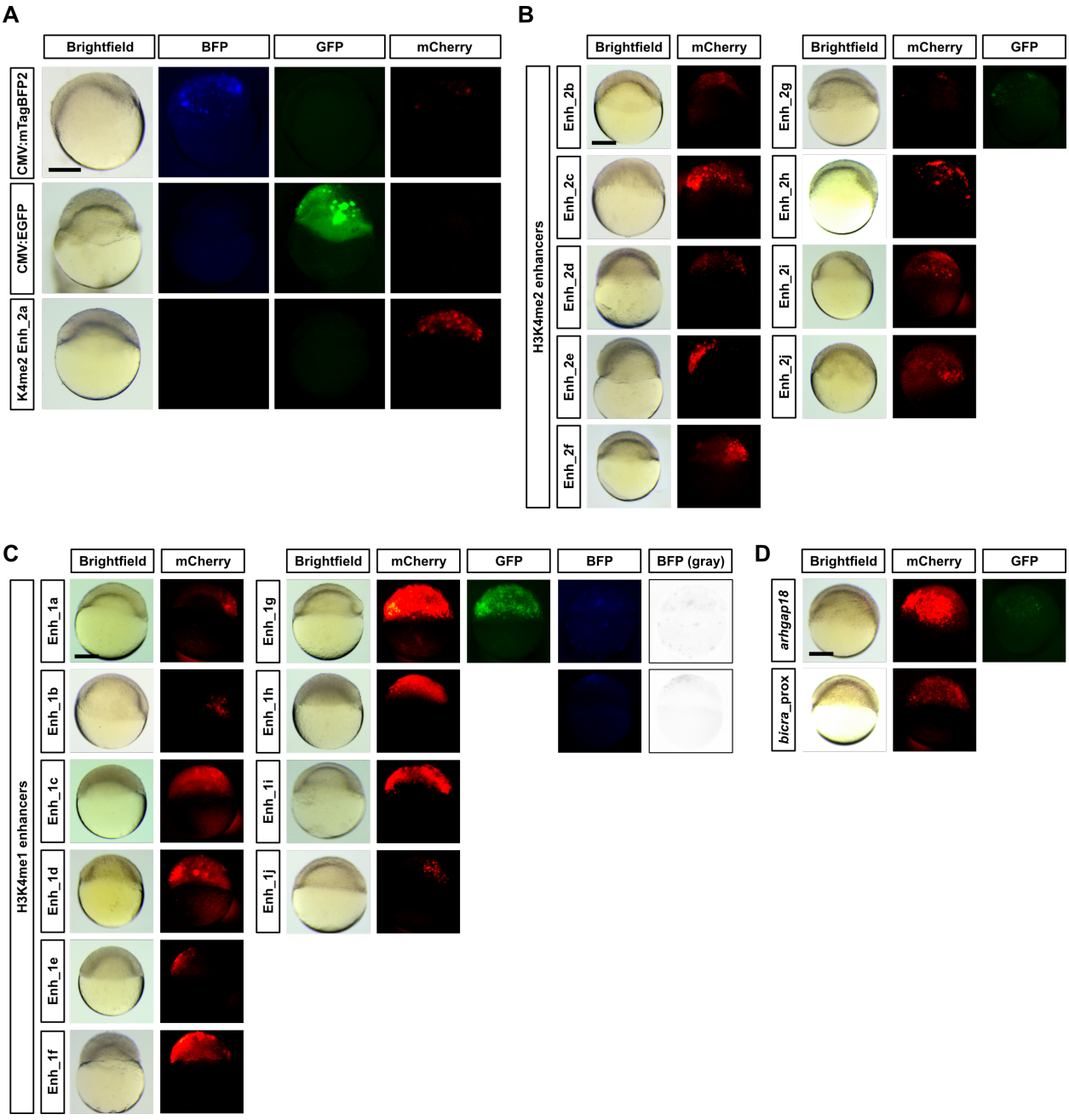

Supplementary Figure 3. Reporter assays for regulatory elements. (A) Representative embryos injected with reporter plasmids (top to bottom, CMV promoter oriented toward the mTagBFP2, CMV promoter oriented toward the EGFP, and H3K4me2 reporter Enh_2a) imaged in brightfield and BFP, GFP, and mCherry channels. Counts are reported in Supplementary Table X. **(B, C)** Representative embryo fluorescence for additional mCherry-positive enhancers. Panels for reporters additionally yielding GFP and/or BFP fluorescence are also shown. BFP fluorescence in these embryos was weak, so grayscale versions of the BFP images are also shown. Enhancers Enh_2i and Enh_2j are the *ier5l* enhancers tested in the CRISPR-Cas9 experiments. **(D)** Representative embryos for a promoter (*arhgap18*) reporter and an element proximal (< 2kb) to the *bicra* TSS, both showing mCherry fluorescence. Scale bar = 250 μm.

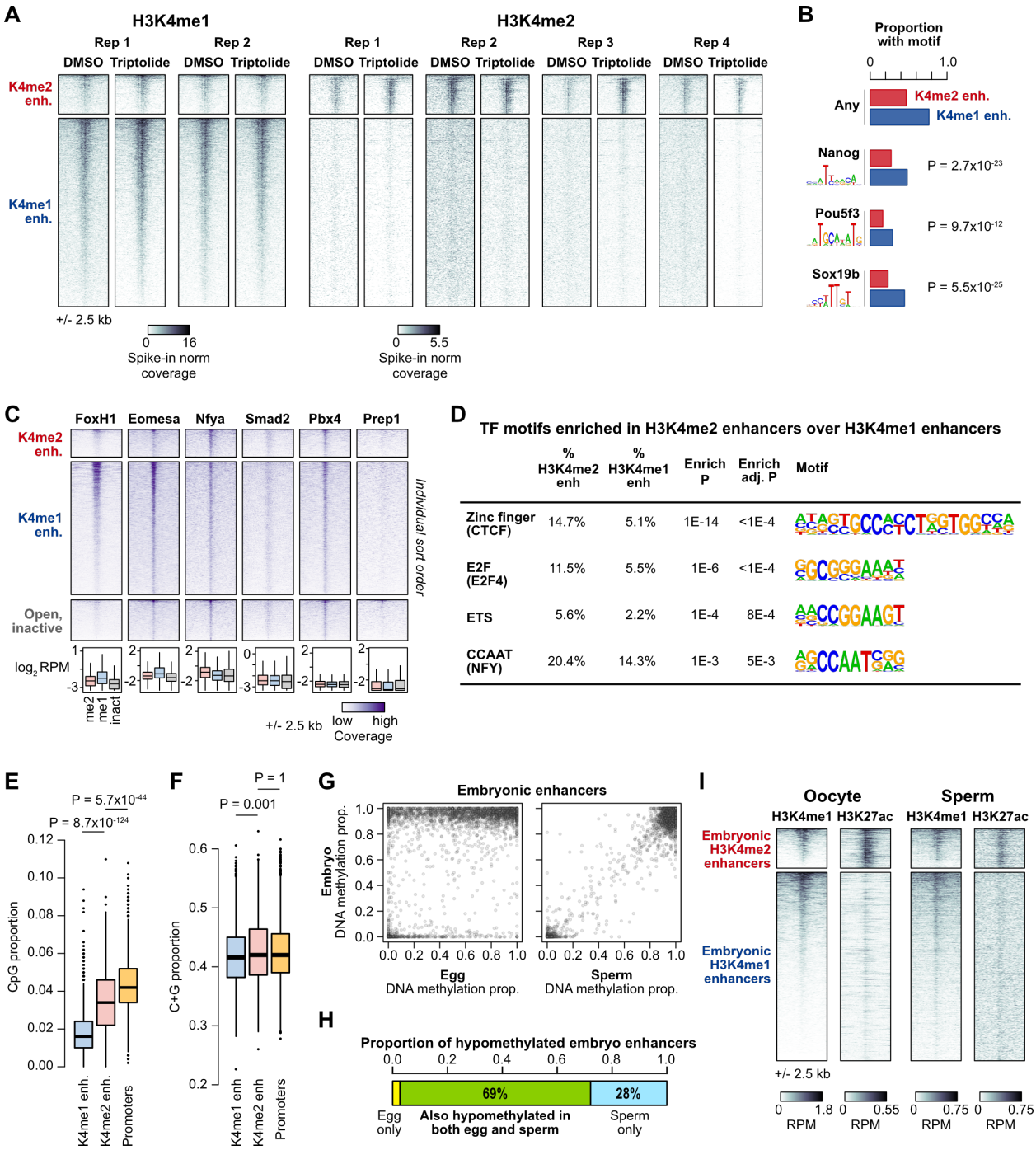

Supplementary Figure 4. Chromatin characteristics of the two enhancer classes. (A) CUT&RUN heatmaps as in Fig. 4A showing individual replicates. Each replicate is a paired DMSO control and triptolide treatment group. **(B)** Barplots showing proportion of enhancers containing predicted zebrafish Nanog, Pou5f3, and Sox19b binding sequences as represented by sequence logos (left) empirically determined from ChIP-seq (data from Miao et al, 2022). P values for Chi-squared tests (2 d.o.f.) are listed on the right. (cont'd...)

(cont'd) **(C)** Heatmaps showing ChIP-seq coverage for different embryonic transcription factors on enhancer regions as well as 1000 ATAC-seq open regions lacking enrichment for any dome-stage histone modifications. Each heatmap is individually sorted in descending order per group. Boxplots summarizing coverage are below each heatmap (boxes are first through third quartiles, center bar median, whiskers extend to 1.5x the interquartile range, outliers are not shown). Data are from Dubrulle et al, 2015 (dome stage FoxH1 and Smad2), Miao et al, 2022 (sphere stage Nfya and Eomesa), Ladam et al, 2018 (high/oblong stage Prep1), Stanney et al, 2020 (high/oblong-stage Pbx4). **(D)** Table of top enriched transcription factor binding motifs in H3K4me2 enhancers relative to H3K4me1 enhancers. One representative motif per family is shown. **(E, F)** Boxplots showing CG dinucleotide (CpG) and C+G nucleotide prevalence in 500 bp centered on H3K4me1 enhancers, H3K4me2 enhancers, and active TSSs. P-values for Wilcoxon rank sum tests are shown. **(G)** Biplots comparing DNA methylation proportion in gametes (x axes) versus sphere stage embryos (y axes) for predicted enhancers. **(H)** Stacked barplot showing the proportion of hypomethylated (<20% methylated) embryonic enhancers that are also hypomethylated in gametes. **(I)** Gamete H3K4me1 and H3K27ac ChIP-seq heatmaps over embryonic enhancers. Data from Murphy et al, 2018 (sperm H3K4me1) and Zhang et al, 2018.

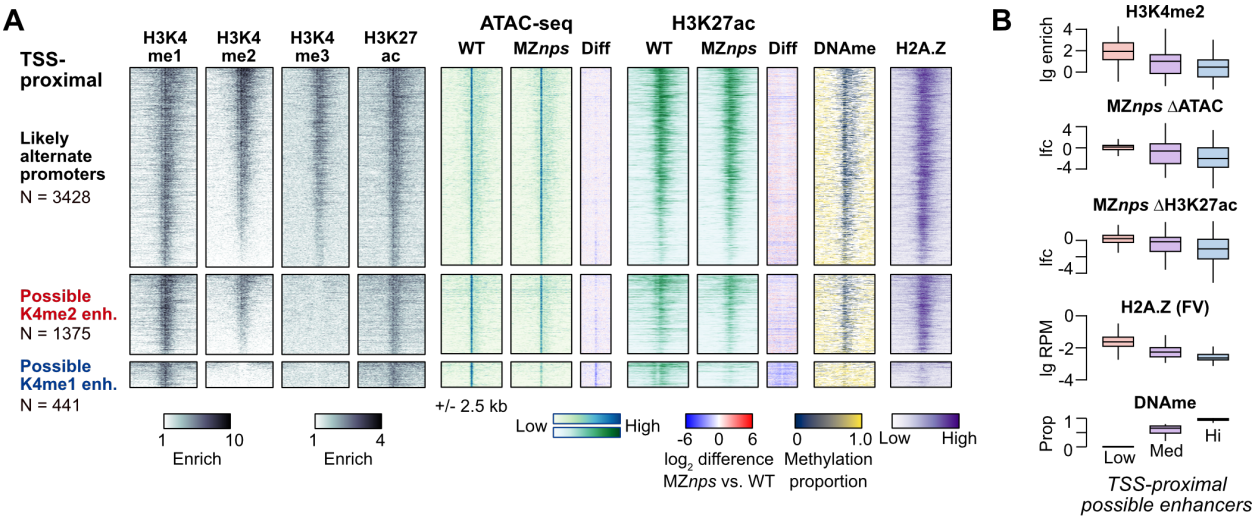

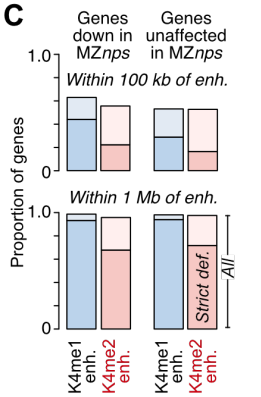

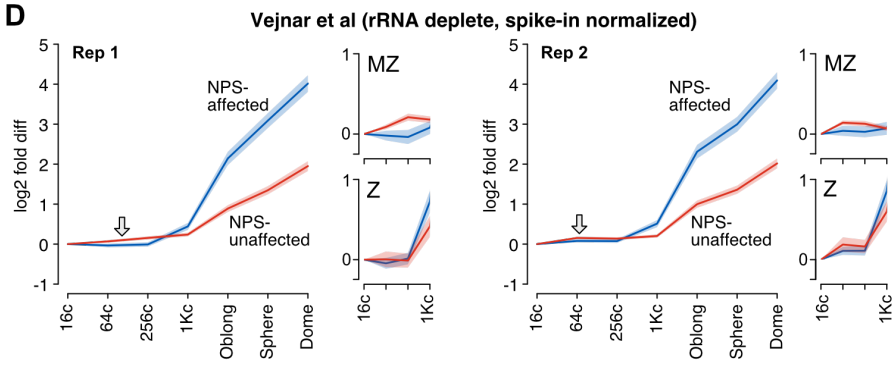

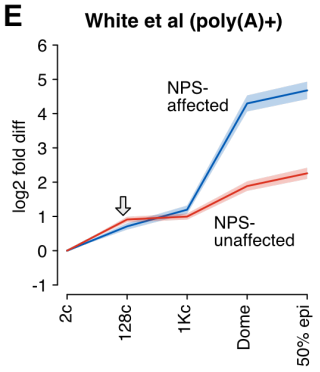

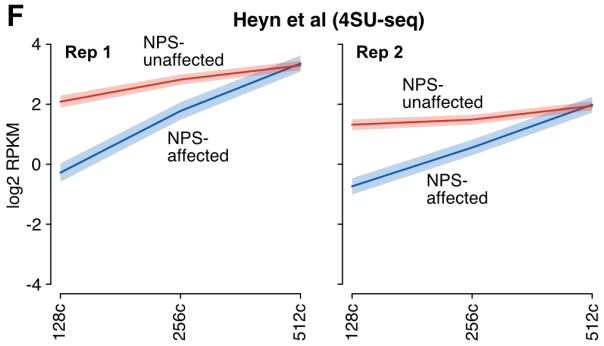

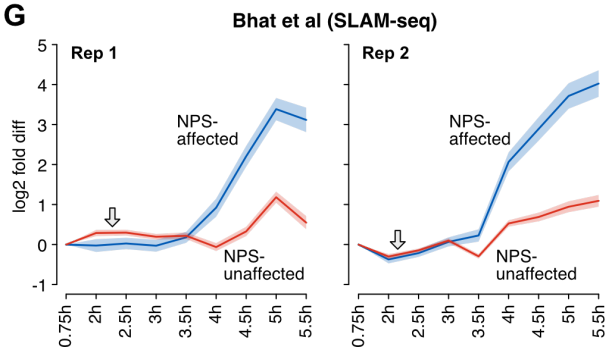

Supplementary Figure 5. Enhancer association with zygotic genes. (A) Expanded enhancer annotations: similar to Fig. 4, heatmaps of chromatin features over TSS-proximal elements excluded from the main enhancer analysis (<2 kb from, but not overlapping, any TSS, regardless if there is evidence for zygotic expression). Elements with H3K4me3 enrichment (top) are considered to be alternate promoters. The remaining elements segregate into possible H3K4me2 enhancers (middle group) and possible H3K4me1 enhancers (bottom group). Reporter assays suggest that such promoter-proximal regions can function as enhancers, despite the ambiguity in annotating them as such (Supp. Fig S3D). **(B)** Boxplots similar to Fig 4E summarizing the correlated chromatin features for TSS-proximal possible enhancers, which likewise segregate into hypermethylated, NPS-dependent, exclusively H3K4me1-marked enhancers and hypomethylated, non NPS-dependent, H3K4me2-marked enhancers. **(C)** Bar plots showing proportion of genes with 100 kb (top) or 1 Mb (bottom) of H3K4me1 enhancers (blue bars) and H3K4me2 enhancers (pink bars). Darker shaded region of each bar represents proportions limited to only strictly defined enhancers (TSS distal and <1.25-fold or ≥3-fold enriched for H3K4me2 for H3K4me1 and H3K4me2 enhancers, respectively). Lighter shaded regions include TSS-proximal elements. **(D-G)** Plots of average wild-type RNA-seq $\log_2$ fold increase over time as in Fig. 5C. MZ = maternal-zygotic genes only, Z = strictly zygotic genes only. Data are from Vejnar et al, 2019, White et al, 2017, Heyn et al, 2014, and Bhat et al, 2023.

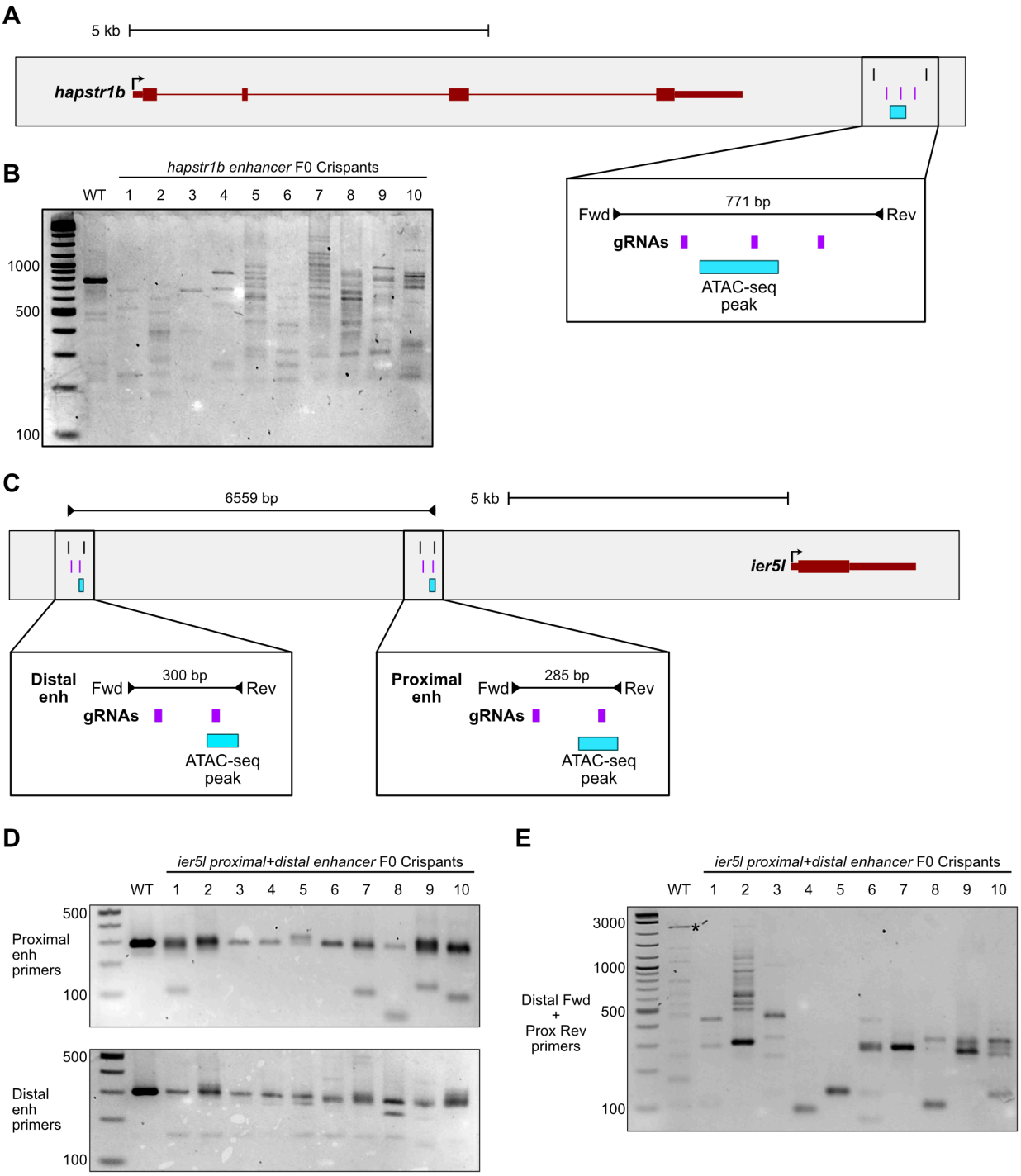

Supplementary Figure 6. Genotyping F0 enhancer crispants. (A) *hapstr1b* locus showing the ATAC-seq open region, CRISPR guide RNA target sites, and genotyping primers at the predicted downstream enhancer region. **(B)** Genotyping gel for single embryos at 32 hours post fertilization. Lane 1 = NEB 1kb Plus ladder, lane 2 = wild-type, lanes 3-12 = embryos injected with a pool of Cas9 complexed with each *hapstr1b* enhancer guide RNA. **(C)** *ier5l* locus showing two upstream predicted enhancers annotated as in (A). **(D)** Genotyping gels for single embryos using primers to detect lesions in the proximal enhancer (top) and distal enhancer (bottom). Crispants were injected with a pool for all gRNAs targeting both enhancers. Gel configuration similar to (B). **(E)** Genotyping gels for the same embryos as in (D) to detect large deletions spanning the two *ier5l* enhancers. The wild-type product (6559 bp) should not efficiently amplify under the PCR conditions used. Bands appearing in the wild-type lane are likely off-target products (asterisk).

Supplementary Table 1. CUT&RUN samples generated in this study

Supplementary Table 2. Regulatory regions defined in this study

Supplementary Table 3. Enhancer reporters

Supplementary Table 4. Sources of public data used